



Non-Contact Tabletop Mechanical Testing of Ultra-High Temperature Ceramics

Zachary N. Wing
Advanced Ceramics Manufacturing
Sindhura Gangireddy, John. W. Halloran
University of Michigan

MAY 2012
Final Report

THIS IS A SMALL BUSINESS TECHNOLOGY TRANSFER (STTR) PHASE II REPORT.

SBIR Data Rights Legend (DFARS 252.227-7018) "SBIR DATA RIGHTS: Contract No. FA9550-10-C-0046. (Advanced Ceramics Manufacturing, LLC, 7800A S. Nogales Highway, Tucson, AZ 85756-9645). In accordance with DFARS 252.227-7018, expiration of SBIR Data Rights is five years after completion of the project, including any follow-on phases. The Government's rights to use, modify, reproduce, release, perform, display, or disclose technical data or computer software marked with this legend are restricted during the period shown as provided in paragraph (b)(4) of the Rights in Noncommercial Technical Data and Computer Software-Small Business Innovation Research (SBIR) Program clause contained in the above-identified contract. No restrictions apply after the expiration date. Any reproduction of technical data, computer software, or portions thereof marked with this legend must also reproduce the markings."

DISTRIBUTION STATEMENT A
DISTRIBUTION A. Approved for public release; distribution is unlimited.

AIR FORCE OFFICE OF SCIENTIFIC RESEARCH
875 N. Randolph St.
Arlington, VA 22203
UNITED STATES AIR FORCE

REPORT DOCUMENTATION PAGE				Form Approved OMB No. 0704-0188	
<small>The public reporting burden for this collection of information is estimated to average 1 hour per response, including the time for reviewing instructions, searching existing data sources, gathering and maintaining the data needed, and completing and reviewing the collection of information. Send comments regarding this burden estimate or any other aspect of this collection of information, including suggestions for reducing this burden, to Department of Defense, Washington Headquarters Services, Directorate for Information Operations and Reports (0704-0188), 1215 Jefferson Davis Highway, Suite 1204, Arlington, VA 22202-4302. Respondents should be aware that notwithstanding any other provision of law, no person shall be subject to any penalty for failing to comply with a collection of information if it does not display a currently valid OMB control number. PLEASE DO NOT RETURN YOUR FORM TO THE ABOVE ADDRESS.</small>					
1. REPORT DATE (DD-MM-YY) 15-05-12		2. REPORT TYPE Final		3. DATES COVERED (From - To) 15 March 2010 – 14 March 2012	
4. TITLE AND SUBTITLE Non-Contact Tabletop Mechanical Testing of Ultra-High Temperature Ceramics				5a. CONTRACT NUMBER FA9550-10-C-0046	
				5b. GRANT NUMBER	
				5c. PROGRAM ELEMENT NUMBER	
6. AUTHOR(S) Sindhura Gangireddy, John W. Halloran, Zachary N. Wing				5d. PROJECT NUMBER	
				5e. TASK NUMBER	
				5f. WORK UNIT NUMBER	
7. PERFORMING ORGANIZATION NAME(S) AND ADDRESS(ES) Advanced Ceramics Manufacturing University of Michigan 7800A S. Nogales Highway Dept. of Materials Sci. & Engin. Tucson, AZ 85756 Ann Arbor, MI				8. PERFORMING ORGANIZATION REPORT NUMBER	
9. SPONSORING/MONITORING AGENCY NAME(S) AND ADDRESS(ES) Air Force Office of Scientific Research 875 N. Randolph St. Arlington, VA 22203				10. SPONSORING/MONITORING AGENCY ACRONYM(S) AFOSR	
				11. SPONSORING/MONITORING AGENCY REPORT NUMBER(S)	
12. DISTRIBUTION/AVAILABILITY STATEMENT DISTRIBUTION A. Approved for public release; distribution is unlimited					
13. SUPPLEMENTARY NOTES This is a Small Business Technology Transfer (STTR) Phase II report developed under topic AF08-T004. Report contains color. Supervision performed by Lawrence Matson, WPAFB, Materials and Manufacturing Directorate, AFRL/RXLN					
14. ABSTRACT A 2 nd generation creep test system was developed referred to as an EMMA-2 (Electro-Magnetic Mechanical Apparatus). EMMA-2 is capable of performing rapid, low cost Creep measurements at temperature >2200°C. The system exploits non-contact Lorentz forces to mechanical flexural loads. This system enables Ultra High Temperature Materials of interest for hypersonics to be easily characterized. Testing was performed on ZrB ₂ -SiC UHTCs. Creep parameters were extracted and found to be in agreement with published data reported at lower temperatures.					
15. SUBJECT TERMS STTR, UHTC, Ultra High Temperature Ceramics, Hypersonic, Creep, Ceramic,					
16. SECURITY CLASSIFICATION OF:			17. LIMITATION OF ABSTRACT: SAR	18. NUMBER OF PAGES 49	19a. NAME OF RESPONSIBLE PERSON (Monitor)
a. REPORT Unclassified	b. ABSTRACT Unclassified	c. THIS PAGE Unclassified			19b. TELEPHONE NUMBER (Include Area Code)

20120816034

TABLE OF CONTENTS

List of Figures.....	ii
List of Tables.....	iii
1.0 Summary	1
2.0 Introduction.....	4
2.1 Ultra High Temperature Ceramics.....	4
2.2 Creep / Conventional Creep Testing.....	5
2.3 Oxidation Ribbon Apparatus	5
2.4 Electromagnetism	7
2.5 EMMA Theory: Non-Contact Forces.....	7
3.0 Methods, Assumption, and Procedures.....	9
3.1 UHTC Materials & Processing.....	9
3.2 EMMA Sample Preparations.....	9
3.3 EMMA Creep Testing & Analysis	10
3.4 Post creep microstructural analysis.....	11
4.0 Results and Discussion	12
4.1 EMMA-2 Design and Build.....	12
4.1.1 Magnetic Flux Assembly	14
4.1.2 Digital Gauss meter.....	15
4.1.3 Controlled DC Power Supply	16
4.1.4 <i>In Situ</i> Deflection Measurement	17
4.1.5 Sample Holder Set Up	18
4.2 System Build.....	24
4.3 Creep Deformation Mechanics.....	25
4.3.1 Fixed Ends.....	25
4.3.2 Pinned Ends	25
4.3.3 Fixed End + Pinned End	26
4.3.4. Mechanics Summary.....	26
4.4 Creep Test Procedure.....	28
4.5 Creep Test Results	28
4.5.1 Creep Testing Atmospheres.....	28
4.5.2 Experimental Conditions – Directly Controlled and Creep Relevant Variables	29
4.5.3 Creep Deflection Profile and Strain Rates.....	31
4.5.4 Creep Data in Ambient and Reduced Oxygen Atmospheres.....	32
4.5.5 Validation of Flexural Creep in ZrB_2-SiC	36
4.5.6 Comparison with Conventional Data.....	37
4.5.7 Summary	38
4.6 Post Creep Microstructural Investigation	39
4.6.1 Motivation.....	39
4.6.2 Post Creep Specimens' Microstructure: Air	40
4.6.3 Post Creep Microstructure – Reduced Oxygen Atmospheres.....	43
4.6.4 Post Creep Microstructure – Damage Evidence.....	44
4.6.5 Eutectic Melting in ZrB_2-SiC	46
4.6.6 Summary	47

5.0 Conclusions.....	48
6.0 References.....	49
LIST OF ACRONYMS, ABBREVIATIONS, AND SYMBOLS	49

LIST OF FIGURES

Figure	Page
Figure 1. (a) Schematic of the self-supporting miniature specimen (b) Digital image of a self-supporting miniature specimen.	6
Figure 2. UHT Apparatus (a) The UHT Apparatus and its components, (b) the copper-silver sample holder with the miniature ribbon sample magnification on the box in (a).	6
Figure 3. Uniformly loaded beam with fixed supports.	8
Figure 4. ZrB ₂ -SiC EMMA creep test bar geometry. Gage length 37.5 mm.	10
Figure 5. Sample inspection points (M) of the ribbon gage section.	10
Figure 6. Schematic of axial and transverse cross sections in the ribbon sample.	11
Figure 7. Schematic of post-creep specimen sectioned for study of interior microstructure and grain size measurements.	11
Figure 8. Design overview for EMMA-2 creep system. From left to right and top to bottom: Side view of electro-magnet, sample holder design – 3D view, sample holder dimensions, sample holder inside bracket, current leads in bracket, holder/bracket, and EMMA-2 system.	13
Figure 9. Electromagnet EMU-75 showing the pole pieces, yoke, wheel screw adjusting system and constant DC power supply DPS-175.	14
Figure 10. Magnetic flux density at the center of the 10mm air gap in EMU-75 with 25mm tapered pole pieces as a function of current in the coils. The maximum flux density achieved was 1.5 Tesla, 50% larger than that by untapered/flat pole pieces.	15
Figure 11. Digital gauss meter – Model DGM 103 showing the probe and the display.	16
Figure 12. Temperature Control Loop with pyrometer to measure the temperature of ribbon and feed it to PID controller that sends corresponding error signal to DC power supply to modify the current for resistive heating of the ribbon.	16
Figure 13. PID controller with DC power supply during a heating test at 1500°C. Both the set value and the measured value indicate the same number since the steady state was reached.	17
Figure 14. Schematic of a triangulation laser measurement system that can measure the movement along line of sight direction (Left). Reflected laser detection in a CCD (Right).	18
Figure 15. Schematics of the slide-in design of the new sample holder set up illustrating both the components, Part-1 and-2. Part-2 is attached to the yoke of the electromagnet where as Part-1 is detachable and can slide onto Part-2 surface with electrical contact points.	19
Figure 16. The first version of Part-1 made from brass support pillars and Phenolic. The grooves in the brass pillars fit the sample as well as the lids. The thumbscrew passing through the bracket, behaves like a c-clamp, and fastens the ribbon inside the groove.	19
Figure 17. Version 2 of Part-1 with reduced thermal conduction made from thin copper pillars with attached silver plates on which the ribbon is fastened with alligator clips/high temperature solder.	20
Figure 18. A 37.5mm long ribbon specimen before creep with 50 Amps corresponding to a temperature of 2150°C and 20 MPa stress.	20
Figure 19. Oxygen concentration in the chamber as a function of time for various amounts of inlet gas flow rates where "a" is the ratio of gas inlet rate and vacuum pump suction rate.	22
Figure 20. Measured oxygen concentration inside the chamber as a function of time with inlet gas flow rate = 6 SCFH.	23
Figure 21. Complete EMMA-2 system.	25
Figure 22. Summary of the stress and the strain conditions in the ribbons under distributed load (w= 1B) with different support systems.	27

Figure 23. Predicted shape of the ribbon after elastic deformation under an equal distributed load with different end supports.	27
Figure 24. (a) Ribbon specimen before creep (b) Specimen after 8 seconds creep with 50 Amps and 0.36T corresponding to a temperature of 2150 °C and 20 MPa stress in non-oxidizing atmosphere. The deflection was 1.25mm corresponding to a strain of 0.28%.	31
Figure 25. Image of deformed ribbon illustrating the error caused by including the contribution from thick ends to the deflection calculation.	31
Figure 26. Deformation profile of a sample while undergoing creep at 1650 °C under 45 MPa stress. Measurements were taken using the laser micrometer.	32
Figure 27. 1600°C under 45 MPa stress (a) center deflection δ_{max} as a function of time (b) Corresponding plastic strain. Slope of the graph was taken to be the creep strain rate of $1.7 \pm 0.1 \times 10^{-5}$ /sec.	32
Figure 28. Creep strain rates of ZrB ₂ -30% SiC in air at 1700 – 2200°C under 20-50 MPa	33
Figure 29. Logarithm of creep strain rates of ZrB ₂ -30% SiC in air at 1700 – 2200°C as a function of logarithm of stress.	34
Figure 30. Creep strain rates of ZrB ₂ -30% SiC in oxidation suppressed atmosphere of N ₂ - 0.25% O ₂ at 1600-2000°C under 30 -50 MPa stress.	35
Figure 31. Comparison of creep strain rates of ZrB ₂ -30% SiC in oxidizing and non oxidizing atmospheres at 50 MPa stress. The creep rates in air corrected to compensate the higher true stresses are also marked.	35
Figure 32. Comparison of EMMA creep data with conventional data acquired through 3-point and 4-point flexure.	37
Figure 33. Secondary electron image of the oxide scale in a specimen creep tested at 1800°C under 38 MPa stress in Air for 300 seconds to a creep strain of 0.37%.	41
Figure 34. Cracks between ZrO ₂ and porous ZrB ₂ oxide scales of sample creep tested in air at 1700°C under 30 MPa stress to a final strain of 0.445%.	41
Figure 35. Cracks developing into delamination in the sample resistively heated in air to 2000°C.	42
Figure 36. X-Ray Diffraction pattern of the surface of the oxide scale of a sample creep tested in air.	43
Figure 37. X-Ray Diffraction pattern of the surface of the sample creep tested in reduced oxygen atmosphere.	43
Figure 38. Specimen tested at 2000°C under 50 MPa stress for 75 seconds to a final strain of 0.86% in air with 0.25% O ₂	44
Figure 39. Secondary electron image of the cross section of sample creep tested at 2000°C under 50 MPa stress in 0.25% O ₂ to a final strain of 0.86% near tensile surface shows no damage in ZrB ₂ or SiC grains.	45
Figure 40. Grain lengths of ZrB ₂ (Left) and SiC (Right) grains along thickness and length directions in tensile, center and compressive regions of the flexure.	46
Figure 41. Eutectic in the ZrB ₂ -SiC Phase Diagram at 2207°C.	46
Figure 42. Secondary electron image of the lamellar microstructure from eutectic melting at 2210°C.	47

LIST OF TABLES

Table	Page
Table 1. Summary of test conditions. Stress and strain calculations based on sample deformation mode.	30

1.0 Summary

Conducting creep characterization using conventional test systems is limited to temperatures on the order of 1500-1700°C. Temperature limits are due to the thermal limits of fixturing needed to support and deliver mechanical loads. The physical contact of the sample requires fixtures that are prone to reaction at these temperatures. Further, costs associated with sample geometries and testing are expensive. These problems have slowed the development and characterization of Ultra High Temperature Ceramics (UHTCs) for hypersonic applications that need to be tested beyond 2200°C. The solution to this problem requires a non-contact method that uses low cost samples.

To circumvent these limitations, our research team proposed a novel method to heat and mechanically load small samples via Lorentz forces. Our Phase I effort was successful in building a crude device called an Electro-Magnetic Mechanical Apparatus (EMMA-1). EMMA-1 leveraged the inherent electrically conductive properties of UHTCs to resistively heat small ribbon samples with high current. Mechanical loads suitable for creep experiments were achieved by placing the heated sample between two permanent magnets to yield a Lorentz force on the sample.

During the Phase II effort, a new design (EMMA-2) was developed to expand and improve the test system's function, develop creep testing process, and to validate the system by conducting a series of creep testing on a relevant UHTC.

EMMA-2's key design improvements were driven by the limitations of EMMA-1 which included: limited magnetic flux density control due to permanent magnets, no environmental control (no control of oxidation), and indirect displacement measurements. The EMMA-2 prototype was completed at the University of Michigan. EMMA-2 now incorporates an electro-magnet, a laser deflectometer, a gauss meter, a dedicated DC power supply, basic environmental control, and each component is mounted into a rigid assembly. These system upgrades allow improved control of test variables (current, magnetic flux density, temperature, and oxidation) and improved data acquisition of sample deflections.

Operational capabilities have been benchmarked on $\text{ZrB}_2\text{-SiC}$ (30 V%) samples produced by ACM. Sample geometry was refined. Using these samples, EMMA-2 has systemically tested samples from 1700-2200°C and 20-50 MPa in air and a "starved air" environment. Testing $\text{ZrB}_2\text{-SiC}$ composites at higher temperatures was not possible due to a eutectic formation. Creep parameters (stress exponents and activation energies) were extracted from our recorded data sets. Activation energies were 139 ± 3 KJ/mol and 148 ± 2 KJ/mol for air and oxygen "starved air," respectively. The stress exponent was 1.4 ± 0.2 . The apparent creep rate was slightly faster in air due to reduction in the load bearing substrate during oxidation. Comparatively, the creep parameters extracted from EMMA-2 testing were in agreement with published (conventional) lower temperature test data.

The test system developed meets many of the criteria/goals established during the original proposal period. EMMA-2 test samples are small (~0.15 cc in volume) and easily manufactured using conventional surface grinding methods (low sample cost). Samples are resistively heated using ~30-100 Watts to reach ultra high temperatures (low electricity costs). Mechanical forces are non-contact in nature. Finally, operational capabilities of EMMA-2 should be able to reach or exceed 2400°C for suitable test materials.

EMMA-2 has established the first rapid, low cost method for conducting creep testing of materials at UHT (Ultra High Temperature). The phase II project has established a firm theoretical and experimental basis from which other UHT mechanical characterization may be performed. Our research team recommends follow on funding to develop additional EMMA-2 test modules capable of evaluating: quasi-static mechanics, fatigue, fast fracture, elasticity, and erosion.

Key Personnel

1. Dr. Zachary Wing, Advanced Ceramics Manufacturing, Director of Science & Technology
2. Professor John Halloran, University of Michigan
3. Dr. Sindhura Gangireddy, University of Michigan, Ph.D. dissertation completed under effort

Publications

1. S. Gangireddy, J.W. Halloran, Z.N. Wing, Creep of Zirconium Diboride –Silicon Carbide up to 2200°C, Submitted to J. Amer. Cer. Soc., September 2011.
2. S. Gangireddy, J.W. Halloran, Z.N. Wing, Non-contact mechanical property measurements at ultrahigh temperatures, J. Eur. Cer. Soc. 30 (2010) 2183–2189.

Presentations

1. S. Gangireddy, J.W. Halloran, Z.N. Wing, A Novel High Temperature Mechanical Characterization Technique, MS&T Conference October 19, 2011.
2. S. Gangireddy, J.W. Halloran, Z.N. Wing, High Temperature, Non-contact, Electromagnetic Mechanical Apparatus for Creep Testing, SEM Annual Conference & Exposition on Experimental and Applied Mechanics, Uncasville, CN, June 2011.
3. S. Gangireddy, J.W. Halloran, Z.N. Wing, Non-Contact Creep Characterization of ZrB₂-SiC Composites with the Electromagnetic Mechanical Apparatus (Invited)," 35th International Conference & Exposition on Advanced Ceramics & Composites, Daytona Beach, FL 2011.
4. S. Gangireddy, J.W. Halloran, Z.N. Wing, Non-Contact Ultra High Temperature Creep Apparatus, National Space & Missile Materials Symposium, **Poster**, Scottsdale, AZ, June 2010.
5. S. Gangireddy, J.W. Halloran, Z.N. Wing, Non-Contact Mechanical Characterization of UHTCs at Ultrahigh Temperatures, AFOSR Contractors Meeting, Arlington, VA, Feb. 2010.

6. S. Gangireddy, J.W. Halloran, Z.N. Wing, Non-Contact Mechanical Testing of Conductive Materials at Ultra High Temperatures Using Electromagnetic Forces, Materials Science & Technology Conference & Exhibition, Pittsburgh, PA, Oct. 2009.

2.0 INTRODUCTION

2.1 Ultra High Temperature Ceramics

Ultra High Temperature Ceramics (UHTCs) are the materials for which this technique was originally invented. UHTCs are a broad class of refractory materials including transition metal borides, carbides and nitrides e.g. ZrB_2 , HfB_2 , ZrC , HfC , TaC , HfN and ZrN . They recently captured interest as potential materials to be used in supersonic and hypersonic vehicles as reusable thermal protection systems and other components. The designs of these future generation vehicles incorporate sharp aero-surfaces that require reliability in the extreme re-entry environments, like oxidizing atmospheres, at very high temperatures.

Refractory borides like ZrB_2 and HfB_2 have extremely high melting temperatures (over $3000^\circ C$), along with other desirable properties like high thermal conductivity, high hardness, retained strength and chemical stability at elevated temperatures. But borides are very poor in oxidation resistance, due to the nature of their oxides: Non-protective ZrO_2 or HfO_2 and volatile liquid B_2O_3 . Addition of SiC to these materials can greatly improve their oxidation resistance by the formation of a passivating layer of silica on the outer surface. SiC addition has also been found improve densification during sintering, thermal shock resistance and room temperature strength without sacrificing high temperature strength. HfB_2 has a slightly higher melting point, but ZrB_2 has the additional advantages of a lower theoretical density and better thermal shock resistance. It is less expensive and has higher thermal conductivity to allow more energy to be conducted away. Therefore, ZrB_2-SiC has been considered a potential UHTC candidate for these applications.

The UHTCs can also operate as structural components for a range of other short and long lifetime applications. Short lifetime applications include weapons system components such as rocket nozzles, nosetips, and leading edges for hypersonic missiles and hypersonic flight vehicles. The long lifetime applications include turbine, missile launchers, guns, and others. Despite intense recent research efforts, UHTCs are still far from being used routinely as hypersonic aero-surfaces because some do not have the required set of properties and the microstructure-processing property relationship is still not well understood. The latter is particularly true of the high-temperature mechanical properties in the creep and pre-creep regimes. Most studies on UHTCs have centered on investigating lower temperature sintering, resistance to oxidation and thermal shock, and room temperature mechanical properties.

Both non-eroding rocket nozzles and sharp leading edges for hypersonic vehicles require materials that will survive service conditions over $2200^\circ C$ for minutes to hours. Meeting these needs will require significant improvements in our fundamental understanding of the response of materials at such high temperatures, especially their resistance to creep. However, conventional methods for measuring creep of these materials have severe limitations that often restrict designers to extrapolating properties from lower-temperature tests. EMMA is designed for mechanical testing of UHTCs at extreme temperatures using non-contact loading using electromagnetic Lorentz forces by exploiting the fact that UHTCs are metallic conductors.

2.2 Creep / Conventional Creep Testing

Creep characterization is necessary for developing design and predictive lifetime estimates for hypersonic vehicles and rocket nozzles. Characterization is most commonly performed by axially loading samples in tension or compression and recording the evolution of strain as a function of time, temperature, and stress.

ASTM C1291 is a standard method for measuring tensile creep in monolithic ceramics. The standard calls for "button-head" or "dogbone" samples geometries. The button-head geometry is a cylindrically gauged end buttons or flanges for fixturing. Approximate dimensions of the test sample are 12 mm in diameter and <165 mm in length. Such geometries must be prepared with a precision cylindrical/universal grinder. The "dogbone" geometry has a flat/rectangular cross section. It has approximate dimension of 80-100 mm in length, 16-20 mm wide, and 2.5 mm thick. The gage section is 2.5 mm wide. For fixturing, "dogbone" samples have holes machined into both ends for load pins. These fixtures are further complicated by the need to deal with heat transfer from the test region to the "grip" region. In both cases, significant machining is necessary. This can be particularly costly in the case of UHTCs which are extremely hard and require expensive diamond and/or electro-discharge machining.

Strain measurements in the standard test methods may be performed using contact extensometers. Non-contact optical methods are also used to measure strain, however, they require the use of "flags" attached to the sample. In either case, secondary materials must contact the specimen and must be at least as refractory as the test material and unreactive with the test material.

Machining, fixturing, and strain measurements all lead to complex and expensive testing of high temperature creep. Fixturing and strain problems become more problematic as temperatures increase. For UHTMs, temperature regimes of interest may exceed 2000°C. Hence, conventional methods and materials do not work.

2.3 Oxidation Ribbon Apparatus

With previous funding from ONR, Karlsdottir and Halloran at the University of Michigan developed a unique "ribbon apparatus" where a small sample of UHTC is self-heated electrically in a low power (100 watts) table-top apparatus. They used it for oxidation studies, and showed that it reproduces what is seen in conventional oxidation tests. With it they observed that formation of the protective scale is dominated by liquid flow of a boron-silica-zirconia liquid.

The table-top ribbon apparatus has been in use at Michigan since 2005 for a variety of UHTC materials. The table-top apparatus is capable of heating conductive UHTC materials to high and ultra-high temperatures (900-2500°C). Test samples consist of simple self-supporting beams, with a thin ribbon machined in their middle. The ribbon section forms a test section that is heated via I²R effects. The thick ends stay cool (and therefore do not react with the surroundings), while the thin ribbon reaches any pre-set high temperature. About 90 Amps of current is passed through the sample, which rapidly heats the ribbon region to incandescence.

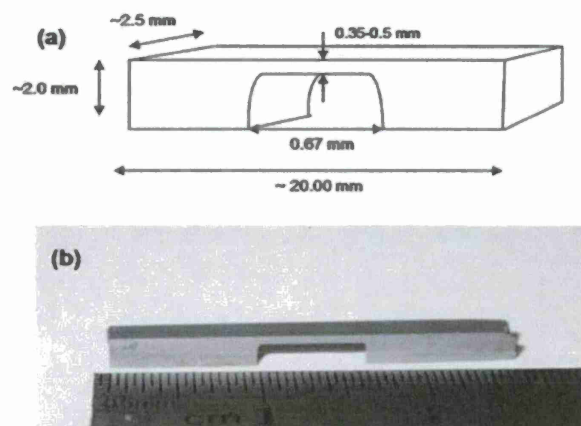


Figure 1. (a) Schematic of the self-supporting miniature specimen (b) Digital image of a self-supporting miniature specimen.

The specimens, as illustrated in Figure 1, are made from a 2.0 mm thick specimen by machining the center region to leave a ribbon about 0.35 mm thick. Convenient ribbon samples can be obtained from ordinary flexure bars used for conventional mechanical testing, although larger samples are easily done as well. A simple surface grinder can be used to prepare many UHTC ribbon samples at once. The UHT oxidation apparatus is shown in Figure 2.

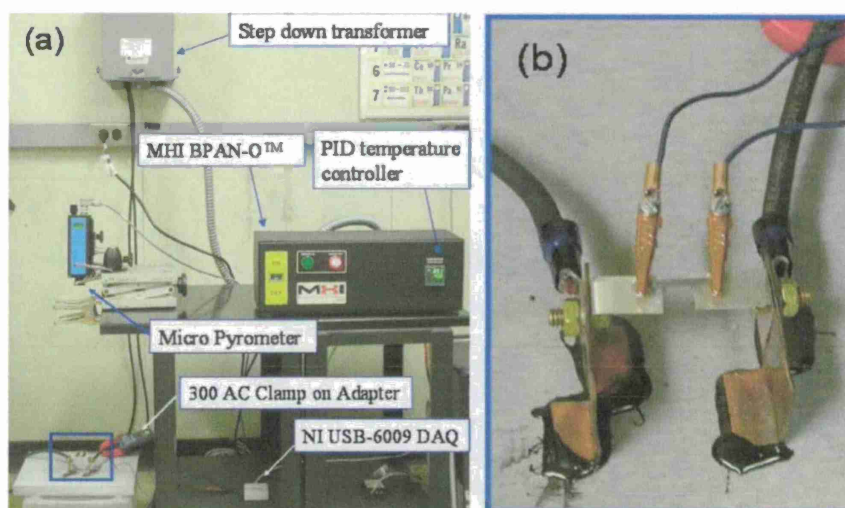


Figure 2. UHT Apparatus (a) The UHT Apparatus and its components, (b) the copper-silver sample holder with the miniature ribbon sample magnification on the box in (a).

A major feature of the Ribbon Apparatus is that very high temperatures (1600-2200+°C) can be achieved at quite low power (~100 watts). This is because only a tiny fraction of the sample is being heated. Low power also implies low heat load to the surroundings, so that instruments can be brought close to the white-hot ribbon without damage.

2.4 Electromagnetism

Electromagnetism is one of the fundamental forces of nature arising from the interaction of electrically charged particles. The Lorentz force is the force on a point charge due to electromagnetic fields, given in terms of the electric and magnetic fields by the following equation:

$$F = q[E + (v \times B)]$$

where F is the force (N), E is the electric field (V/m), B is the magnetic field (T), q is the electric charge of the particle (C) and v is the instantaneous velocity of the particle (m/s). In the absence of electric field,

$$F = q(v \times B)$$

This could be rewritten for a current carrying conductor in purely magnetic field as $F = I \times B$. Since $q \cdot v = I$, a moving charge is equivalent to current. When the ribbon specimen is resistively heated, all that is required to create a mechanical load is the application of a magnetic flux density B , to create a Lorentz force per unit length

$$F = I \times B$$

If the current is applied in the x-direction along the length of a sample L_T , and the magnetic flux density is applied from the sides in the y-direction, there will be a distributed mechanical load (w in N/m) directed vertically in the z-direction: $w_z = I_x B_y$.

For example, if the current required to heat the ribbon is 50 amps and the applied magnetic flux density is 10,000 G (or 1 T or 1 N/m-A), there will be a uniform loading $w=50$ N/m. The total force on a 30 mm long specimen ($L_T = 0.030$ m) will be 1.5N, or about 0.34 pounds of force.

2.5 EMMA Theory: Non-Contact Forces

The Electro-Magnetic Mechanical Apparatus (EMMA) exploits the basic electromagnetism theory that explains the Lorentz force. Ribbon apparatus samples are heated by a current I . Therefore, a mechanical load may be applied by a magnetic flux density B , to create a Lorentz force per unit length $F = I \times B$.

Now consider the geometry of the UHTC Ribbon Specimen, as illustrated in Figure 1a. This is a small bar UHTC specimen, such as a standard ASTM "B-bar" used for flexural testing, with thickness t_T , width Y and total length L_T . The center section is machined away to leave a ribbon of length L and thickness t . The ribbon is the hot section. It is supported by the thicker ends (the cold support). When an electrical current I passes down the length of the specimen, the current density is low in the cold support (current density $= I/Yt_T$) and it remains cool. But the current density is much higher in the thin ribbon (current density $= I/Yt$), and it is heated to incandescence. Thus, a very hot ribbon can be self-supported by its cold ends.

The temperature Θ of the ribbon varies approximately parabolically across the ribbon section, depending on the current I , electrical resistivity $\rho(\Theta)$ at transfer conditions by conduction, convection, and radiation. For very long ribbons in a vacuum where radiation dominates, the temperature varies with current approximately as:

$$\Theta \approx \frac{\beta}{(\rho(\Theta)\epsilon)^{1/4}} I^{1/2}$$

Where ϵ is the emissivity and β involves geometric factors such as surface area.

If the entire specimen is exposed to a transverse magnetic flux density B_y , it will experience a uniform distributed mechanical load w_z , as described above. But the section modulus of the specimen changes dramatically in the thin ribbon section, so that if the cold support ends are held in place, the thin ribbon behaves like a beam of length L with constrained ends. The mechanics of the beam (assuming fixed-fixed conditions) are illustrated in Figure 3.

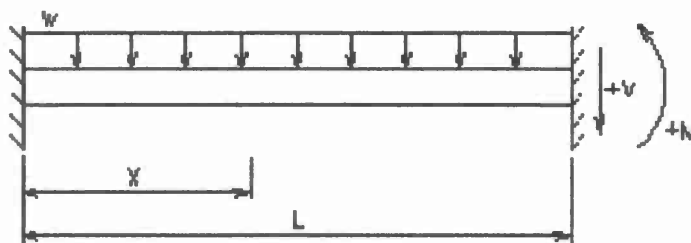


Figure 3. Uniformly loaded beam with fixed supports.

This distributed force w_z creates a moment M in the center of the span given by

$$M = w_z \frac{L^2}{16}$$

This creates a tensile stress in the outer fiber of the beam given by

$$\sigma_{\max} = \frac{Mc}{I} = \frac{Mt}{2I} = \frac{Mt}{2 \frac{Yt^3}{12}} = \frac{w_z L^2}{16} \frac{6}{Yt^2}$$

and since the distributed force $w_z = I_x B_y$, the maximum flexural stress on the ribbon is related to the current, magnetic flux, and ribbon dimensions by:

$$\sigma_{\max} = 0.250 \frac{L^2}{Yt^2} (I_x B_y)$$

For a typical case where $I = 100$ amps, and $B = 0.5$ Tesla (or 0.5 N/Am or 5000 Gauss), with a ribbon with $L = 25$ mm, $Y = 2$ mm and $t = 0.2$ mm, the maximum stress is about 150 MPa. This is sufficient to cause significant creep deflection at 1500°C or above for most ZrB_2 -SiC composites, based on Inna Talmy's data.

Now the current I_x cannot be changed without changing the temperature Θ so in order to vary the stress at constant temperature, either the magnetic flux or specimen dimensions must change. We can approximately model to express the current as an implicit function of temperature:

$$I \approx \sqrt{\frac{\rho\varepsilon}{\beta}} \Theta^2$$

Which can be substituted into the expression for stress to give:

$$\sigma_{\max} \approx 0.250 \sqrt{\frac{\rho\varepsilon}{\beta}} \Theta^2 \left[\frac{L^2}{Yt^2} \right] B_z$$

With the EMMA method, both the Lorentz force and the temperature depend upon current, so applied stress and temperature cannot be independently varied.

3.0 METHODS, ASSUMPTION, AND PROCEDURES

3.1 UHTC Materials & Processing

Advanced Ceramics Manufacturing prepared the ZrB_2 -30 V% SiC composite by hot pressing. UHTC raw materials were obtained from commercial sources: ZrB_2 (HC Stark Grade B) had a particle size 1.5-3 μm and SiC (H.C. Stark Grade UF10) had a particle size of 0.7 μm .

Powders were prepared by ball milling powders for 24 hours in iso-propyl alcohol using WC milling media. Powders were dried using a rotovap and sieved after milling. Samples were consolidated into billets $\sim 7 \times 80 \times 80$ mm inside a resistively heated, uni-axial, graphite hot press. Hot pressing was performed at the following conditions: vacuum, 28 MPa, 2100°C, and 30 minute soak time. A heating rate of 5°C/min was used.

The hot pressed material had a ZrB_2 grain size of $2.52 \pm 0.45 \mu m$ and SiC grain size of $1.61 \pm 0.28 \mu m$. Four point (ASTM C1161 "B" bars) flexural strength of the UHTC samples is typically 664 MPa. The density of the UHTC samples was 5.34 g/cc (102% that of theoretical). The four point resistivity of this material was measured to be $2.66 \times 10^{-7} \Omega\cdot m$.

3.2 EMMA Sample Preparations

ZrB_2 -SiC plates were surface ground and sectioned into sample blanks $\sim 2.5 \times 2.5 \times 37.5$ mm. The test bars were abrasively machined to size using a CNC surface grinder. Samples were rough machined using a 100 grit diamond wheel and finished to size using a 380 grit diamond wheel. The specimens were prepared in ribbon geometry as shown in Figure 4 with ribbon dimensions

37.5 mm × 2 mm × 0.35-0.50 mm. Samples were fixtured into sets of four to ensure consistent ribbon thickness across multiple test specimens.



Figure 4. $\text{ZrB}_2\text{-SiC}$ EMMA creep test bar geometry. Gage length 37.5 mm.

Samples were inspected post machining to assess variability and limit dimensional variations influencing creep data. Each test specimen was measured at eight locations (Figure 5, M1-M8) using a precision micrometer. Thickness variations within a single ribbon specimen were on the order of 8 μm .

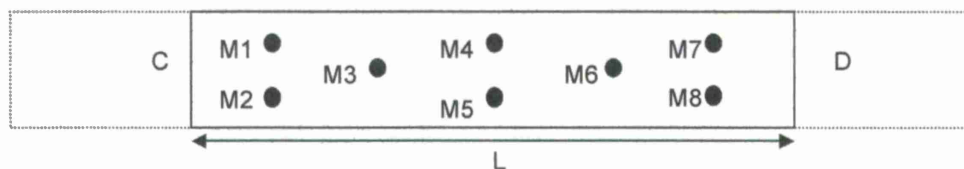


Figure 5. Sample inspection points (M) of the ribbon gage section.

3.3 EMMA Creep Testing & Analysis

Ribbon specimens were heated resistively with a DC current and the temperature was measured with an optical pyrometer. The pyrometer signal was used to control temperature by adjusting the DC current using a PID controller and a programmable DC power supply. The ribbon was exposed to a transverse magnetic flux from an electromagnet. The mechanical load to the specimen was applied without physical contact using the electromagnetic Lorentz force. A current of 45 – 65 Amps was required to heat these UHTC ribbon samples to temperatures 1600-2200°C. Since the current requirement varies with temperature to be able to apply similar loads at different temperatures, the magnetic flux is adjusted accordingly. To apply different loads at a given temperature, the magnetic flux needs to be altered. Creep tests were performed in two environments, ambient air and reduced oxygen atmosphere. In the latter case, the environmental

chamber was purged with compressed nitrogen to achieve a low percentage of remnant oxygen <0.25%, as detected with an oxygen sensor (Illinois Instruments, Model 910, Johnsburg, IL).

3.4 Post creep microstructural analysis

Samples were sectioned and cold mounted in low temperature (80°C) curing epoxy and polished down to 0.25 μm using traditional procedures. From each of these two types of cross sections obtained from a given sample, three areas of 25 μm \times 25 μm size were selected from tensile, center and compressive sides of the ribbon specimen for measurement of ZrB₂ and SiC grain lengths. Figure 6 and Figure 7 illustrate the transverse sectioning of ribbon specimen and the grain size measurement procedure. These cross sections were studied using FEI Quanta 200 3D Scanning Electron Microscope.

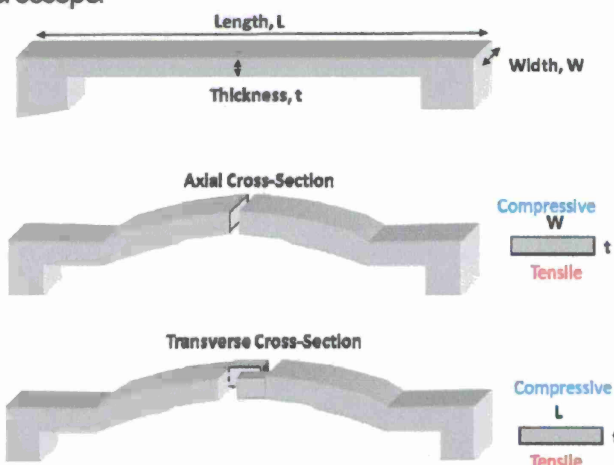


Figure 6. Schematic of axial and transverse cross sections in the ribbon sample.

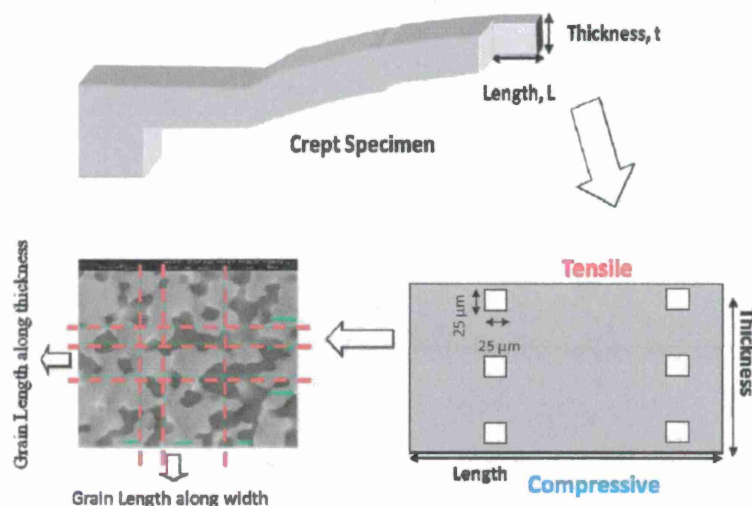


Figure 7. Schematic of post-creep specimen sectioned for study of interior microstructure and grain size measurements.

4.0 RESULTS AND DISCUSSION

4.1 EMMA-2 Design and Build

An upgraded design was conceived based on the Phase I results. The 2nd generation system (EMMA-2) targeted key hardware upgrades which included an electro-magnet, laser micrometer, environmental chamber/control, and improved sample fixturing.

An electro-magnet was selected over a permanent magnet due to its ability to vary magnetic flux and to give the system a wider range of capabilities. A laser micrometer was proposed to automate gathering of creep displacement data in real time compared to the iterative heat/cool down method used in Phase I. An environmental chamber was added to the EMMA system to control/limit oxidation of test samples. The design concept is shown in Figure 8.

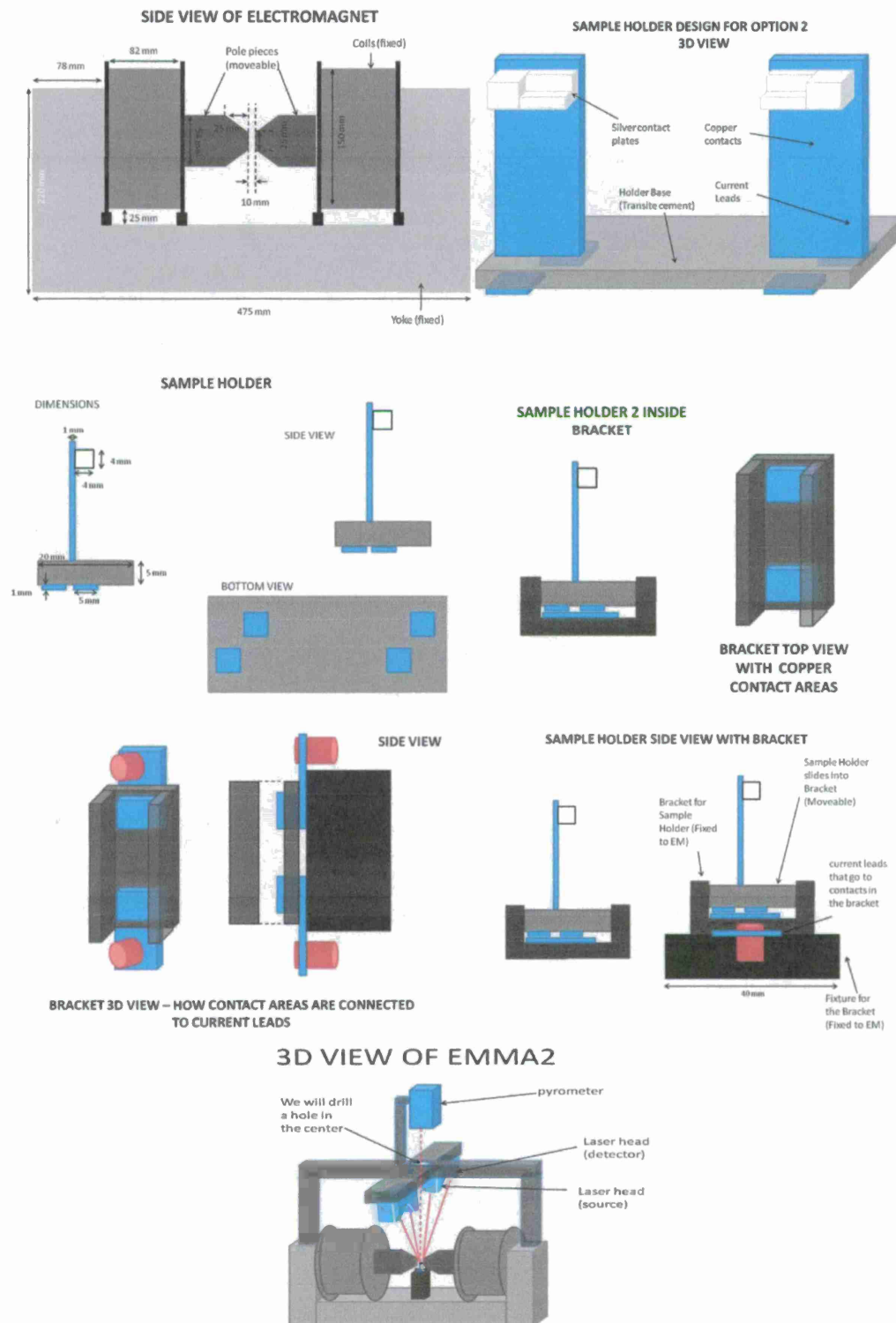


Figure 8. Design overview for EMMA-2 creep system. From left to right and top to bottom: Side view of electro-magnet, sample holder design – 3D view, sample holder dimensions, sample holder inside bracket, current leads in bracket, holder/bracket, and EMMA-2 system.

4.1.1 Magnetic Flux Assembly

In an electromagnet, the magnetic flux density can be varied by changing the air gap distance as well as altering the current passing through the coils. We exercise the latter option. This allows the entire assembly to be fixed in place, hence the possibility to be enclosed, and still manipulate the magnetic flux.

An electromagnet (model EMU-75) was procured from Silicon Valley Science Labs. It has a U-shaped soft iron yoke with dead annealed soft iron pole pieces. The pole pieces are 75mm in diameter. The air gap is continuously variable from 0-75mm with two way knobbed wheel screw adjusting system. The energizing coils are wound on non-magnetic formers with uniform layers of S.E. grade copper wire. A DPS-175 power supply was designed to be used with EMU-75 as a constant current power supply allowing smoothly adjustable current in the range 0-3 Amperes per coil (i.e., a total of 6 Amps). Figure 9 is a photograph of the electromagnet showing the pole pieces, yoke, the wheel screw system and the constant DC power supply that supplies current into the coils. The flat pole pieces would generate a magnetic field up to 10 k-Gauss or 1 Tesla with the maximum 3 Amps current and an air gap of 10 mm.

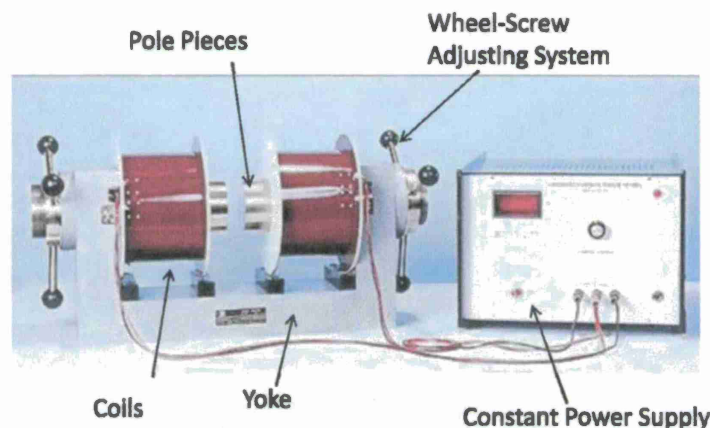


Figure 9. Electromagnet EMU-75 showing the pole pieces, yoke, wheel screw adjusting system and constant DC power supply DPS-175.

To amplify the flux density in the air gap further, the pole pieces were tapered. However, the higher flux density comes at the expense of smaller uniform field space. A balance was struck by having the size of the tapered poles the same as the expected length of ribbons (~ 25mm).

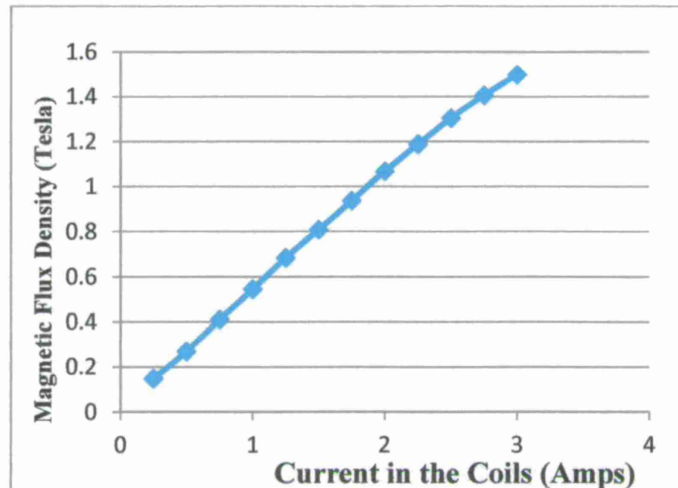


Figure 10. Magnetic flux density at the center of the 10mm air gap in EMU-75 with 25mm tapered pole pieces as a function of current in the coils. The maximum flux density achieved was 1.5 Tesla, 50% larger than that by untapered/flat pole pieces.

The tapered pole pieces resulted in the magnetic flux density of 1.5 Tesla with 3 Amps current and 10mm air gap, a 50% increase from that by untapered/flat pole pieces. The flux density in the center of the 10mm air gap was measured as a function of different amounts of current passed through the coils, as plotted in Figure 10. Magnetic flux density at the center of the 10mm air gap in EMU-75 with 25mm tapered pole pieces as a function of current in the coils. The maximum flux density achieved was 1.5 Tesla, 50% larger than that by untapered/flat pole pieces.. Compared with the magnetic flux assembly of EMMA-1 which could reach only 0.34 Tesla, the flux density in the new electromagnet is 340% larger. Thus, the applied stresses in EMMA-2 can be 4.4 times larger than in EMMA-1.

4.1.2 Digital Gauss meter

The magnetic field in the air gap of an electromagnet is more complex than that generated by the permanent magnets. Therefore, theoretically calculating the flux density at a given location in the air gap is not easy. A digital gauss meter based on the Hall Effect in semiconductors is employed to empirically measure the flux density at the ribbon location. It operates on the principle that a semiconductor carrying current develops an electromotive force when placed inside a magnetic field, in a direction perpendicular to the direction of both electric current and magnetic field. The magnitude of this E.M.F. is proportional to the field intensity if the current is kept constant.

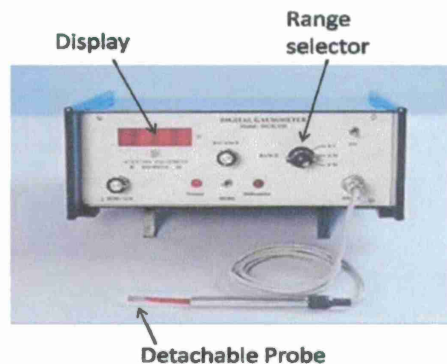


Figure 11. Digital gauss meter – Model DGM 103 showing the probe and the display.

The DGM-103 model can measure in the range 0-20 k-Gauss with a resolution of 1 Gauss.

4.1.3 Controlled DC Power Supply

The DC current supply utilized in EMMA-1 was not only borrowed, but also manually operated. A pyrometer was utilized to measure the temperature of the ribbon surface and the current was adjusted accordingly by hand. The manual operation limited the extent of control and relatively large temperature fluctuations of the order of $\pm 50^{\circ}\text{C}$ were inevitable. This situation was remedied by a control-loop (Figure 12) with a PID controller to modify the current driven by the DC power supply to maintain constant temperature of the ribbon.

Figure 12. Temperature Control Loop with pyrometer to measure the temperature of ribbon and feed it to PID controller that sends corresponding error signal to DC power supply to modify the current for resistive heating of the ribbon.

The control loop consists of the pyrometer reading the temperature of the ribbon and feeding it to the PID controller, which then depending on the difference between this measured value and the set point, generates an error signal to give out a control output to the DC power supply and it modifies the output current accordingly. We use a Eurotherm PID temperature controller, model 2408, and Mikron Infrared pyrometer, model MS-140, that can measure from $900\text{--}3000^{\circ}\text{C}$. The current required to heat the ribbon specimen from $0\text{--}3000^{\circ}\text{C}$ ranges between 0-60 amperes. However, the UHTC materials (being highly conductive) require small voltages 2-4 volts even

for the long ribbons. Therefore, the power supply should operate in small voltages and large amperage.

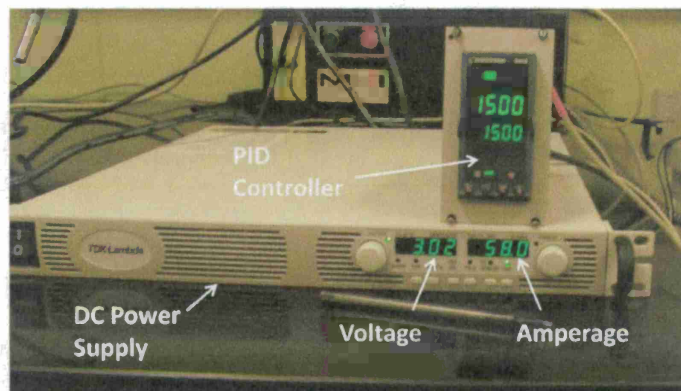


Figure 13. PID controller with DC power supply during a heating test at 1500°C. Both the set value and the measured value indicate the same number since the steady state was reached.

A 1500W TDK-Lambda DC Power Supply, model Genesys Gen 12.5-120 was obtained. It operates in 0-120 Amps and 0-12.5Volts completely suitable for our heating requirements.

4.1.4 Deflection Measurement

In conventional flexural creep tests, the fixture that applies the load has a location sensor and tracks the mid span deflection as the sample deforms. However, the fixtures being in contact with the hot material place a major limitation on temperature of testing. EMMA was designed to overcome these constraints by working with non-contact forces which allow operation at UHT. Therefore, any deflection measurement system that can be used in EMMA has to be non-contact as well. Previously in EMMA-1, the mid-span deflection was measured after the creep test. To have *in situ* deflection measurement is more practical because a single isothermal, iso-stress test can collect the required information compared to several such experiments with varying time durations if the measurements are made after the test.

Laser triangulation sensors determine the position of a target by measuring reflected from the target surface. A "transmitter" (laser diode) projects a laser spot on the target, and its reflection is focused via an optical lens on a light sensitive device or "receiver". If the target changes its position from the reference point, the position of the reflected spot of light on the detector changes as well. The schematic of triangulation laser measurement system is depicted in Figure 14.

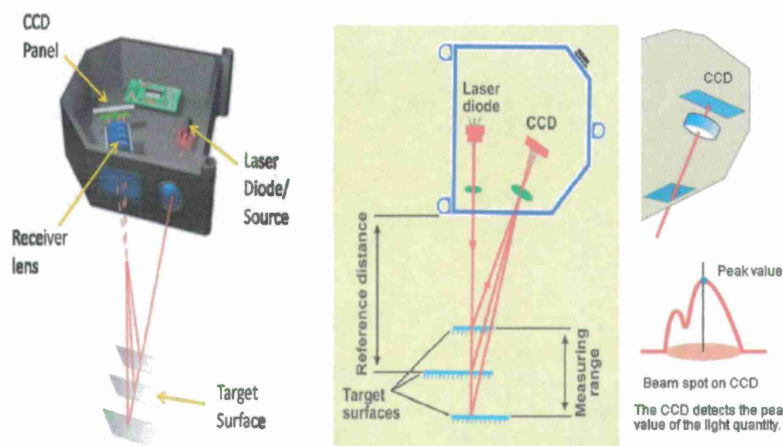


Figure 14. Schematic of a triangulation laser measurement system that can measure the movement along line of sight direction (Left). Reflected laser detection in a CCD (Right).

When such a triangulation laser micrometer is used for high temperature applications, there is another radiation involved, i.e. the incandescence or the electromagnetic radiation of the hot objects. Thus, the light reaching the CCD panel is composed both of the reflected laser and that of incandescence. Since the CCD cannot discern between the two, proper laser function depends on the dominating radiation. If the laser power exceeds the incandescent radiation reaching the CCD, the pixels where the laser hits still record the highest intensity and the incandescence becomes background noise (laser performance will be accurate). On the other hand, if the incandescence is larger, the pixel which is closest to the hot object or “sees” most of that radiation is identified as the spot (the output of the location of the target surface corresponds to this wrong pixel) and the laser will not be able to establish the target surface.

Thus, the comparison of laser power with incandescent radiation is critical to the viability of laser micrometers as an *in situ* deflection measurement system for EMMA. Commercially available class-II lasers have a power of $\sim 5\text{mW}$, which can be operated in the open. Classes of lasers with higher energies will have to be accompanied by extreme safety gear.

A regular industrial red laser from Keyence (model LK-G 157) was evaluated. It was capable of establishing the position of a ribbon sample surface at 1600°C , but at 1750°C the higher incandescence lead to erroneous results. However, a shorter wavelength laser was found to eliminate the incandescence effect. A high accuracy blue laser sensor, model MRL-DS, working at a wavelength of 405nm with an inbuilt optical filter was procured from Metrology Resource Co. This particular model has a resolution of 10 microns (however, more expensive models with resolution $< 1\text{micron}$ are also available). This *in situ* measurement technique provides efficient data collection and higher resolution than a manual optical technique.

4.1.5 Sample Holder Set Up

The first ribbon holder design was envisioned to be a slide-in design with two separable components, part-1 and part-2 the schematics of which are illustrated in Figure 15.

Figure 15. Schematics of the slide-in design of the new sample holder set up illustrating both the components, Part-1 and-2. Part-2 is attached to the yoke of the electromagnet where as Part-1 is detachable and can slide onto Part-2 surface with electrical contact points.

Part-1 consists of two supports (Part 1-A) to hold up the ribbon in the gap between them. Their bases are attached to an electrically insulating and high temperature (400°F) resistant material like Transite cement board or MACOR or Phenolic (Part 1-B). These supports are not simply standing on this board, but pass through slots made in it and glued with high temperature (450°F) epoxy. Therefore they leave two electrical contact points underneath Part-1.

Two versions of Part-1 were contrived. The first endeavor, depicted in Figure 16, was two brass pillars with grooves for the thick ends of the sample to sit in. It has two brass lids (that also can fit into the slots) to hold the sample in the groove. An L-bracket fitted to the brass pillar has a thumbscrew to apply vertical force on each lid and fasten the ribbon like a C-clamp.

Figure 16. The first version of Part-1 made from brass support pillars and Phenolic. The grooves in the brass pillars fit the sample as well as the lids. The thumbscrew passing through the bracket, behaves like a c-clamp, and fastens the ribbon inside the groove.

However, there was excessive heat conduction through the brass pillars leading to large temperature gradients in the hot zone. As a result, the hot zone was much shorter than the length of the thin test section. This subsequently led to lower stresses that were unable to cause deformation. This problem was solved by reducing the cross-section of the support pillars which linearly reduces the path for thermal conduction. The second version of Part-1, depicted in Figure 17, was made from silver plates attached to thin copper pillars. The sample was fastened using alligator clips.

Figure 17. Version 2 of Part-1 with reduced thermal conduction made from thin copper pillars with attached silver plates on which the ribbon is fastened with alligator clips/high temperature solder.

The temperature profile along the length, measured using the infrared pyrometer at a constant current setting of 50 amperes is shown in Figure 18. The discontinuity is due to the lower limit of the pyrometer being 900°C. A 25mm region of temperature uniformity indicates the fixture related heat conduction losses have been reduced.

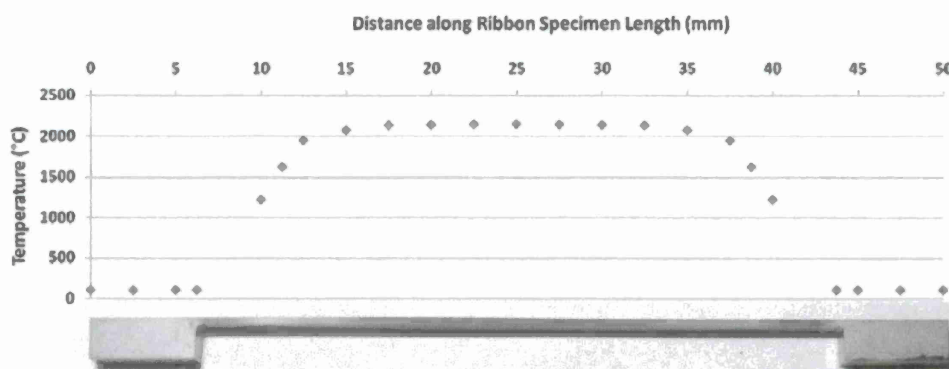


Figure 18. A 37.5mm long ribbon specimen before creep with 50 Amps corresponding to a temperature of 2150°C and 20 MPa stress.

4.1.6 Environmental Chamber

High temperature creep testing in ambient air is typically accompanied by oxidation resulting in the formation of complex oxide scales. Rapid oxidation occurs when performing creep tests above 1800°C. At such high oxidation rates, the thin cross section of the ribbon sample can not last long. Oxidation during creep testing with EMMA has two effects:

1. The duration of the test is limited to the time before the sample is oxidized through its thickness. Since the oxide scales are not electrically conductive like the UHTC, the test will cease.
2. Large oxidation scales change the mechanical behavior of the ribbon itself. The stress and strains during the creep testing in EMMA, and any conventional test, are derived from elastic beam analysis. However, the presence of thick oxide scale on either side of the material and its different mechanical characteristics requires this to be treated as a cladding problem. The oxide scales are typically more brittle and cause faster failure, as was observed in the above mentioned test.

Therefore, it is desirable to have atmospheric control during creep tests that are performed at temperatures above 1700°C (for ZrB₂-SiC) to understand oxidative/non-oxidative effects. This inspired the design and subsequent fabrication of an environmental chamber with controlled atmospheric conditions. This chamber was envisioned to be a completely enclosed space around the sample holder area, where the sample will undergo oxidation. It was made feasible by the slide-in design of the resistive heating set up where the sample holder parts can be completely detached from the rest of the set up with the current leads to the DC power supply.

The environmental chamber required several ports to allow access for the current leads, outlet to vacuum pump, inlets for the target gas, oxygen sensor and pressure meter. It also needed a front door for the slide-in of sample holder and an IR-window on the top for the laser micrometer and the pyrometer to be able to record the sample. Apart from these, there were two large ports on either side were essential to allow the pole pieces of the electromagnet approach close to the sample. This was indispensable since a target air gap of ~10mm is needed to be able to reach high magnetic flux densities of >1 Tesla. Although the design aimed for complete enclosure, there are inevitably several possible locations for leaks to occur in this system and need to be corrected. The amount of oxygen present in the chamber was tracked by an Illinois Instruments Oxygen Analyzer, model 910, and the gas flow designs include an unknown leak rate, \dot{V}_{Leak} . Two different gas flow set ups were attempted to purge the ambient atmosphere inside the chamber and replace it with non-oxidizing gas like Nitrogen. One of these utilized a vacuum pump to aid in the faster purge of the existing atmosphere, and the other gas flow set up relied on gas exchange.

Arrangement 1:

This set up included three major components: a nitrogen cylinder to supply the inlet gas, a vacuum pump that drew the atmosphere in the chamber, and an oxygen sensor to record the oxygen content in the chamber. The inlet gas was connected through a flow meter to regulate the in-gas flow rate. An outlet to the oxygen sensor was fitted with a pressure gauge to read the pressure in the chamber.

The inlet gas flow rate was controlled through the regulator, hence \dot{V}_{inlet} is a user defined variable. The suction rate of the vacuum pump depended on the pressure inside the chamber. But as the pressure gauge did not record any noticeable fluctuation in the internal pressure, \dot{V}_{vacuum} , can be assumed to be a fixed quantity, corresponding to atmospheric pressure. Flow rate through the sensor, \dot{V}_{sensor} , cannot be directly controlled but will depend on the pressure conditions inside the chamber. The flow meter in the sensor records this value. The fourth possible gas flow is the unknown leak rate, which will depend on the other three terms. All the gas flow rates coming into the system (the chamber) are counted positive and those going out as negative. Since no fluctuations in the chamber pressure were monitored, the gas flow is at balance as shown below.

$$\dot{V}_{inlet} - \dot{V}_{vacuum} - \dot{V}_{sensor} \pm \dot{V}_{Leak} = 0$$

The sign of the leak rate term will depend whether the incoming gas flow is relatively larger or smaller than the outgoing flow. Let " a " be the ratio of gas inlet rate and vacuum pump suction rate, ————. When ———— is set smaller than ————, i.e. $a < 1$, the system exists under slight vacuum and leak rate is positive with ambient air leaking into chamber. When ———— or $a > 1$, the leak rate is negative and the atmosphere inside the chamber leaks to the atmosphere.

The gas exchange process inside the chamber can be treated as a Continuously Stirred Tank Reactor (CSTR) problem. The volume (V) of the environmental chamber is $2 \times 10^{-3} \text{ m}^3$ and the vacuum pump rate ———— was measured to be $4 \times 10^{-5} \text{ m}^3/\text{s}$. Based on these values, the oxygen concentration as a function of time for the two cases is given by:

$$\begin{aligned} & \text{————— for } a < 1 \\ & \text{————— for } a \geq 1 \end{aligned}$$

Figure 19 compares the results of these two scenarios in the plot of oxygen concentration as a function of time for different values of a . When $a < 1$, since ambient air is leaking in there is a lower limit on the oxygen concentration $= 0.2(1-a)$, as can be seen from the plot. Whereas $a > 1$ ensures leak rate is negative and oxygen content will fall exponentially with time.

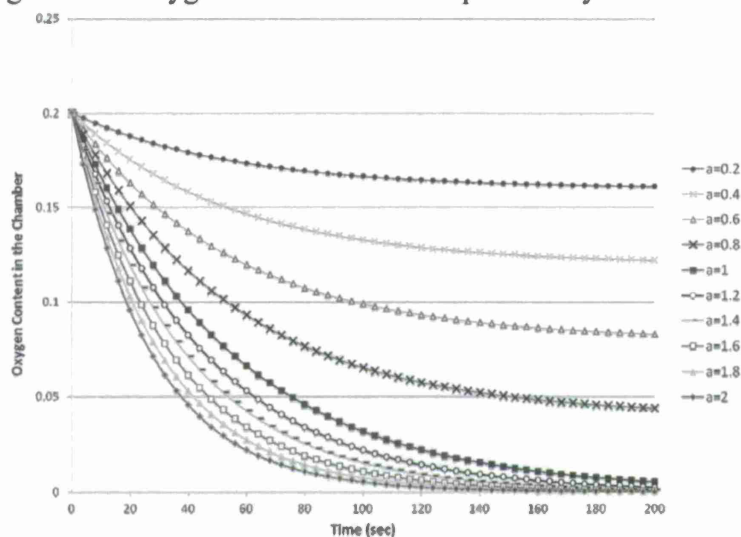


Figure 19. Oxygen concentration in the chamber as a function of time for various amounts of inlet gas flow rates where " a " is the ratio of gas inlet rate and vacuum pump suction rate.

Arrangement 2:

A simpler set up was investigated by removing the vacuum pump and setting the nitrogen inflow rate larger than the gas flow rate going out through the sensor. This ensured the leak rate would be negative. This second approach relies entirely on a gas exchange process to purge the chamber of oxygen with incoming nitrogen gas. Since the oxygen sensor had no pump, the flow

rate of the gas going out through the sensor, was much smaller than the incoming gas flow rate, . As a result the system is under slight positive pressure which causes any leak rates to be negative or going out of the system. The flow balance is shown below.

If this arrangement is also considered as a CSTR problem, it is estimated to have an oxygen concentration as a function of time is given by:

which is similar to the second case scenario arrangement 1. So either of the two set ups can be used to purge the ambient air with desired atmosphere. Figure 20 shows the empirical oxygen content measured by the oxygen analyzer as a function of time for $a=1.2$, i.e. gas inlet rate of 6 SCFH or $4.8 \times 10^{-5} \text{ m}^3/\text{s}$.

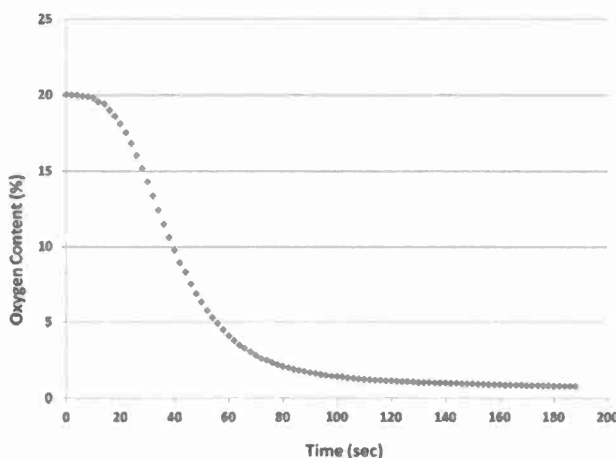


Figure 20. Measured oxygen concentration inside the chamber as a function of time with inlet gas flow rate = 6 SCFH.

With the incoming gas as Nitrogen, the steady state oxygen content could be brought under 0.2% which is sufficiently low to suppress oxidation of the UHTC materials. Other gases like Ar+5% H_2 could also be used to replace the air in the chamber and bring the Oxygen concentration even lower at shorter time durations. While Argon is considered non-reactive with UHTCs even at high temperature, Hydrogen would react with the oxygen in the chamber to form water vapor. The reactivity of oxygen with hydrogen is greater than that with hot UHTC and therefore the presence of hydrogen would prevent oxidation of the material. 5% Hydrogen is under the explosive limit. On the other hand water vapor is considered to affect the stability of the oxide scale of UHTC. Both B_2O_3 and SiO_2 forming compounds such as $\text{Si}(\text{OH})_4(\text{g})$ suffer volatilization, thereby enhancing the oxidation rate.

An optical window with high transmission was embedded using an O-ring on the top plate of the environmental chamber so as to allow the laser micrometer and the micro-pyrometer to view the sample surface and record its position and temperature respectively. Despite the high transmission, the presence of the window in the optical paths affects the results of both the laser micrometer and the pyrometer.

The laser micrometer readings indicate a shift in the position of the sample surface despite the ribbon sample being stationary. This phenomenon can be explained by the refraction of the laser light at the two surfaces of the optical window. The double diffraction leads to a shift in the location where the laser light hits the CCD sensor and a corresponding shift in the sample positioning is recorded. However, since this shift does not vary with the working distance between the micrometer and the sample, it is not difficult to accommodate for this shift and obtain the real position of the sample from the shifted readings. Similarly, the optical window acts like a filter absorbing and reflecting some of the radiation from the sample from reaching the pyrometer. The pyrometer works by measuring the thermal irradiance from the hot object and identifies the temperature. Suppose the optical window has a transmission of $t\%$, the irradiance seen by the pyrometer would be $t\%$ of the actual irradiance.

$$J_{shifted} = J_{actual} * \frac{a}{100}$$

where J is the irradiance given by $J = \epsilon\sigma T^4$. So,

$$T_{shifted} = T_{actual} * \left(\frac{a}{100}\right)^{1/4}$$

Therefore, an optical window of 91.1% transmission causes the pyrometer temperature to shift by 2.3% from the actual temperature. At elevated temperatures like 1500°C, this corresponds to a difference of 35°C. Therefore, this factor of $\left(\frac{a}{100}\right)^{1/4}$ was accounted for obtaining the exact temperature of the ribbon from the measured value.

4.2 System Build

The components for the initial EMMA-2 prototype were acquired and assembled at Michigan. Figure 21 shows the current EMMA-2 system. It occupies about 2 meters of bench space including the power supply for the electromagnets (on left) and the power supply and control for the DC resistive heating current. The specimen in the environmental chamber, within the sample holder, is in the center between the poles of the electromagnet. The pyrometer for measuring temperature and the laser micrometer for measuring deflection are on rigid vertical supports. These supports are fabricated from standard Aluminum sections and rigidly attached to the heavy iron yoke of the electromagnet.

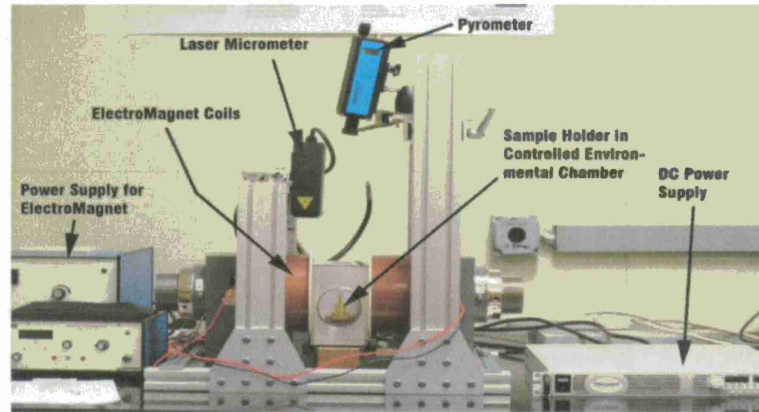


Figure 21. Complete EMMA-2 system.

4.3 Creep Deformation Mechanics

The mechanical behavior of the thin test section acts as a beam whose deformation is highly dependent on the nature of fixation of the ends. The moment generated by the mechanical load and the corresponding reaction moments affect the overall stress state experienced in the ribbon. Three types of behavior were observed during creep testing with the end supports acting as: Fixed-Fixed ends, Pinned-Pinned ends, and Fixed-Pinned ends.

4.3.1 Fixed Ends

If the thick edges of the ribbon are held in place without allowing any lateral movement, the mechanics are similar to a beam with fixed ends.

A fixed end – fixed end beam under distributed load is a commonly studied structural analysis problem. M_R , R_x and R_y are unknown reaction moments and forces generated at the fixed ends, which can be obtained by balance of all the forces and moments in the above free body diagram. The distributed load causes bending moments in the ribbon given by:

$$M(x) = \frac{w_z}{2}x(L - x) - \frac{w_z L^2}{12}$$

where x is the distance from one of the fixed ends. This moment is largest at the center of the span, $M(L/2)$, and the maximum stress in the beam is:

$$\sigma_{\max} = 0.25 \frac{L^2}{YI^2} (I_x B_y)$$

4.3.2 Pinned Ends

On the other hand if the thick edges of the ribbon are allowed any lateral movement, the ribbon behaves very differently and the mechanics are similar to a beam with pinned ends.

A pinned beam under distributed load is also a commonly studied structural analysis problem. These ends do not support any reaction moments and horizontal reaction forces. Therefore, reaction forces are vertical, R_y , which can be obtained by the balance of vertical forces. The distributed load causes bending moments in the ribbon given by:

$$M(x) = \frac{w_z}{2} x(L - x)$$

where x is the distance from one of the ends. This moment is largest at the center of the span, $M(L/2)$, and the maximum stress in the beam is:

$$\sigma_{\max} = 0.75 \frac{L^2}{YI^2} (I_x B_y)$$

Therefore, if the supports are allowed lateral movement, stresses would be three times higher than when restricted.

4.3.3 Fixed End + Pinned End

If one of the thick edges of the ribbon is restricted from any lateral movement and the other edge is allowed to move horizontally, then the ribbon behaves as a fixed-pinned ended beam. Although the mechanics of this situation are less commonly studied, the solutions are straight forward. The distributed load causes bending moments in the ribbon given by:

$$M(x) = w_z x \left(\frac{3L}{8} - \frac{x}{2} \right)$$

where x is the distance from the pinned end. The moment is not largest at the center as was in the previous cases, but instead is largest at $x = \frac{3L}{8}$, the maximum stress in the beam is:

$$\sigma_{\max} = \frac{27}{64} \frac{L^2}{YI^2} (I_x B_y)$$

Maximum stress is smaller than that of a pinned-pinned beam but larger than that in a fixed-fixed beam.

4.3.4. Mechanics Summary

Strain in creep samples was calculated from elastic beam theory. Strain equations were obtained from beam theory for each boundary condition by replacing the Elastic Modulus (E) with $\frac{\sigma(\max)}{\epsilon}$ to relate the strain caused by the flexural bending to the maximum deflection. Values were derived from the maximum deflection measured.

Figure 22 summarizes the stress, strain, and deflection equations for each set of sample boundary conditions.

$$y = \frac{w}{24EI} (x^3 L^2 + x^4 - 2x^3 L)$$

$$\sigma_{max} = \frac{1}{4} \cdot \frac{IBL^3}{bt^3}$$

$$\delta_{max} = \frac{1}{16} \cdot \frac{IBL^4}{24EI}$$

$$\epsilon = 8 \cdot \frac{\delta_{max} t}{L^2}$$

$$y = \frac{w}{24EI} (xL^3 + x^4 - 2x^3 L)$$

$$\sigma_{max} = \frac{3}{4} \cdot \frac{IBL^3}{bt^3}$$

$$\delta_{max} = \frac{5}{16} \cdot \frac{IBL^4}{24EI}$$

$$\epsilon = 4.8 \cdot \frac{\delta_{max} t}{L^2}$$

$$y = \frac{w}{48EI} (xL^3 + 2x^4 - 3x^3 L)$$

$$\sigma_{max} = \frac{27}{64} \cdot \frac{IBL^3}{bt^3}$$

$$\delta_{max} = 0.15 \cdot \frac{IBL^4}{24EI}$$

$$\epsilon = 6.5 \cdot \frac{\delta_{max} t}{L^2}$$

Figure 22. Summary of the stress and the strain conditions in the ribbons under distributed load ($w=IB$) with different support systems.

Maximum stress can be expressed generally as:

$$\sigma_{max} = \chi \frac{L^2}{Yt^2} (I_x B_y)$$

where χ is a fraction 0.25-0.75 depending on the type of end supports.

The result of the creep experiments is the permanent deformation δ_{max} of the specimen which is measured using the laser micrometer from which the strain is derived generally as:

where γ is a number 4.8 or 6.5 or 8 depending on whether the supports are fixed-fixed or fixed-pinned or pinned-pinned type.

Comparison of the strain with respect to maximum deflection in the three support systems, reveals that the value of — is largest for the fixed-fixed beam, followed by pinned-fixed beam, and smallest for pinned-pinned beam. The significance is that although large deflections can occur in pinned beams, the strain is not as high. On the other hand, in the fixed beams the apparent deformation may not be large, but the corresponding strain could be.

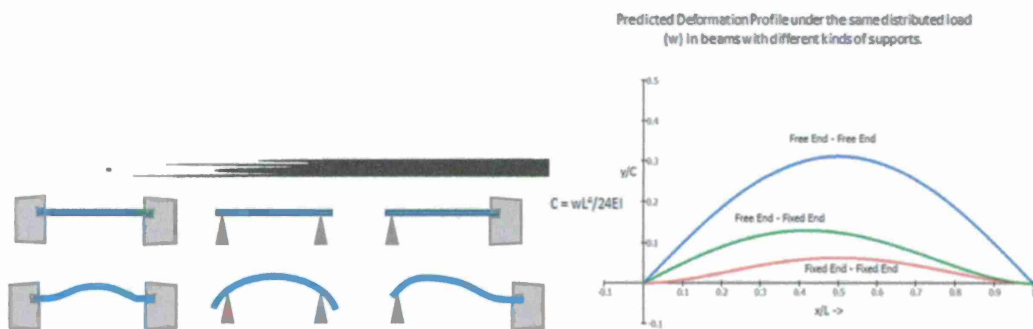


Figure 23 shows the predicted deformation profiles of a ribbon under same amount of distributed load, but with different support systems. This trend can be explained by the fact that the fixed ends generate reaction moments that counter the bending moment caused by the load. The pinned ends cannot support reaction moments, and therefore even a similar load causes larger stresses causing it to deform more. They also do not resist deformation at the edges leading to large y_{max} values. The fixed supports cannot deform at the edges placing further resistance to deformation, leading to smaller y_{max} values. Fixed-free behavior falls midway between the two.

The supports used in EMMA were spring loaded contacts (miniature alligator clips). All three different boundary conditions (deformation profiles) were observed during testing. This is believed to be due in part to the manufacturing variations in the spring constant of the clips.

4.4 Creep Test Procedure

Operation of EMMA involves several steps:

- i) Ribbon sample mounting on sample holder with alligator clips (~ 30 seconds)
- ii) Sample holder inserted into the Part 2-A (~ 15 seconds)
- iii) For controlled atmosphere testing – exchanging ambient air with desired gas (~ 3 minutes)
- iv) Set electromagnet coil current for desired magnetic flux density (~ 15 seconds)
- v) Check alignment of the pyrometer (~ 15 seconds)
- vi) Apply specimen current to reach target temperature (~ 30 seconds)
- vii) Creep test duration (1-5 minutes)
- viii) Cool to room temperature (~ 1 minute)

The entire time duration of a creep test in EMMA is therefore only ~ 5-10 minutes. The total cost of the beta apparatus was approximately \$25,000 and included several components of equipment which were either procured from vendors or custom designed. Major components include an Electromagnet (1.5 Tesla maximum), a Digital Gauss meter to monitor magnetic flux density, a programmable DC power supply with a PID controller, an Infrared Pyrometer to measure the temperature, a violet Laser Micrometer to measure deflection *in situ*, and an Oxygen Analyzer to monitor the oxygen content inside the environmental chamber were purchased from manufacturers. Other components such as the slide-in sample holder, its base, and the environmental chamber were custom designed and manufactured.

4.5 Creep Test Results

4.5.1 Creep Testing Atmospheres

Creep testing of ZrB_2 -SiC in air at high temperatures is inevitably accompanied by oxidation of the material which leads to formation of complex oxide scales. These oxide scales are an outer layer of silica acting as a protective film, a columnar layer of Zirconia, and a porous ZrB_2 layer where the SiC has selectively oxidized and flowed out. As a result of the oxidation process,

direct mechanical properties of pure $\text{ZrB}_2\text{-SiC}$ are not obtained, but instead, the mechanical properties of the oxidized $\text{ZrB}_2\text{-SiC}$ are obtained.

The $\text{ZrB}_2\text{-SiC}$ oxide scales are electrically non-conducting. So at high temperatures, $>2000^\circ\text{C}$, the time duration of a test has to be much shorter to avoid variation in the current required to resistively heat the thin ($<500\text{ }\mu\text{m}$ thickness) ribbon specimens. If the tests are longer than a few minutes duration, the current value will decrease since the current conducting portion thickness is reduced. If the test duration is too long, a sample ribbon can be oxidized through their thickness and then the current flow is stopped bringing the resistive heating to a halt. Therefore, EMMA tests are ceased after only a short duration at very high temperatures.

Oxide products result in a decrease in the thickness of unreacted (load bearing) material since the oxide scales are composed of large amounts of liquid silica and cannot endure significant stresses. Therefore, the oxide scales really do not contribute in stress bearing under the creep test load. So even while the applied load in EMMA is constant, the true stresses in the unoxidized portion of the $\text{ZrB}_2\text{-SiC}$ substrate are higher. In the thin ribbon specimen, oxidation causes a significant reduction in the thickness of the remaining substrate. These higher stresses may lead to higher creep rates in air. To report the creep response of the pure $\text{ZrB}_2\text{-SiC}$, oxidation has to be suppressed.

Understanding both the oxidative and non-oxidative creep behavior of UHTCs are important for hypersonic applications. Fundamentally, material scientists need to determine routes to control or inhibit creep. Modelers also need governing creep data from test conditions that replicate the actual application environment. Therefore creep experiments were performed in air as well as in Nitrogen with small amount of O_2 . Suppression was accomplished by performing the tests inside the environmental chamber in an atmosphere containing mainly nitrogen and a trace amount of oxygen $< 0.25\%$.

4.5.2 Experimental Conditions – Directly Controlled and Creep Relevant Variables

A current of 45-65 Amps was required to heat samples to temperatures $1600\text{-}2200^\circ\text{C}$. The applied magnetic flux density ranged from 0.2 to 0.5 Tesla and was maintained uniformly across the entire length of the ribbon. The directly controllable variables within EMMA-2 are current and magnetic flux through which temperature and stress are indirectly controlled. Table 1 summarizes all the test conditions of creep experiments in the ambient and the low oxygen atmospheres.

Table 1. Summary of test conditions. Stress and strain calculations based on sample deformation mode.

Test No	L [mm]	W [mm]	t [mm]	I [A]	B [T]	Time [s]	δ [mm]	T [°C]	Stress [MPa]	ε [%]
Geometry			(Directly controlled)			Micrometer	Pyrometer	Elastic beam theory		
OXIDIZING ATMOSPHERE										
59	37.5	2.6	0.45	75	0.42	25	1.215	1900	50.4	0.205
61	30	2	0.37	43	0.45	80	0.673	1800	29.4	0.18
64	30	2	0.37	43	0.5	120	0.416	1800	19.84	0.135
71	37.5	2	0.42	50	0.45	33	0.804	2000	20.76	0.19
73	30	2	0.37	40	0.45	300	0.386	1700	21.2	0.105
74	30	2	0.35	43	0.45	49	1.537	2000	28.8	0.4
75	37.5	2.5	0.5	62	0.45	60	1.268	1800	49.1	0.215
80	37.5	2.5	0.5	55.5	0.46	275	2.75	1700	50.25	0.445
81	37.5	2.5	0.5	56.5	0.3	260	1.176	1700	29.7	0.195
88	37.5	2.5	0.5	59	0.22	70	0.825	1900	19.3	0.15
90	37.5	2.5	0.5	60	0.22	50	1.512	1900	30.65	0.22
91	37.5	2.5	0.5	62	0.36	60	2.355	2000	29.1	0.46
92	37.5	2.5	0.5	64	0.36	20	5.834	2100	50.0	0.89
93	37.5	2.5	0.5	64	0.36	18	4.361	2225	30.0	0.865
94	37.5	2.5	0.52	70	0.36	27	2.438	2100	30.0	0.505
95	37.5	2.5	0.52	77	0.28	23	1.859	2200	20.0	0.435
67	30	2	0.35	44.5	0.52	30	1.180	2100	20.0	0.305
72	37.5	2	0.42	45	0.45	300	1.254	1700	33.0	0.250
76	37.5	2.5	0.47	60	0.36	65	1.412	1800	42.5	0.220
82	37.5	2.5	0.52	58	0.20	180	0.225	1700	11.0	0.380
38	37.5	2.5	0.45	56.5	0.38	35	3.875	2000	50.0	0.580
68	37.5	2	0.40	45	0.45	53	0.857	1800	23.0	0.190
NON OXIDIZING ATMOSPHERE										
96	37.5	2.5	0.5	56	0.47	66	1.189	1800	51.73	0.18
101	37.5	2.5	0.5	61	0.36	90	4.173	1900	49.97	0.635
102	37.5	2.5	0.5	60.5	0.36	75	1.573	1900	31.08	0.305
105	37.5	2.5	0.5	62.5	0.36	75	6.015	2000	50.46	0.87
106	37.5	2.5	0.5	63.5	0.22	80	4.294	2000	28.95	0.66
108	37.5	2.5	0.5	53	0.39	240	0.419	1600	48.95	0.065
111	37.5	2.5	0.5	57	0.39	150	0.37	1700	30.16	0.075
113	37.5	2.5	0.5	54	0.39	98	0.633	1800	28.78	0.165

4.5.3 Creep Deflection Profile and Strain Rates

The geometry of the thin section of the ribbon (with its length relatively much longer than its thickness) ensures that the deflection in these specimens (at even small strains) will be easily perceptible. The strains in the post creep specimens were calculated to be in the range of 0.15-0.87%. But due to the geometry, the deformations were significant and usually of the order of 1mm. Figure 24 shows a post creep specimen tested at 2150°C and 20 MPa stress in non-oxidizing atmosphere with a deflection of 1.25mm corresponding to a strain of 0.28%. The deformation was in fixed-fixed end type and hence has a deformation profile where the slope of deflection goes to zero at the ends. It may be noticed that even such a low strain induces appreciable deformation in the long thin ribbons.

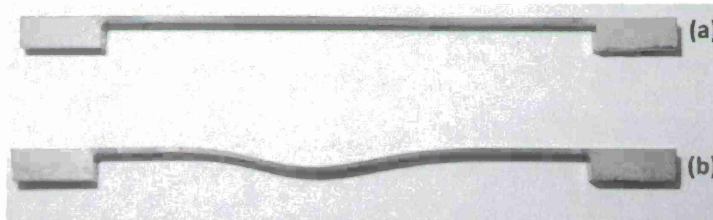


Figure 24. (a) Ribbon specimen before creep (b) Specimen after 8 seconds creep with 50 Amps and 0.36T corresponding to a temperature of 2150 °C and 20 MPa stress in non-oxidizing atmosphere. The deflection was 1.25mm corresponding to a strain of 0.28%.

There were two major types of error possibilities in deriving δ_{\max} from the deflection profile data.

- Fixture end supports were vertically separated by a fraction of a mm. Although neither obvious to the visible eye nor significant to the electromagnetic load, this vertical separation induces considerable variation in the measured maximum deformation, which is itself on order of a millimeter in several creep tests.
- Contributions by the ribbon sample ends occur to δ_{\max} . Figure 25 shows an image of a deformed ribbon illustrating this error.

These two errors were corrected in all the deformation profiles and data analysis.

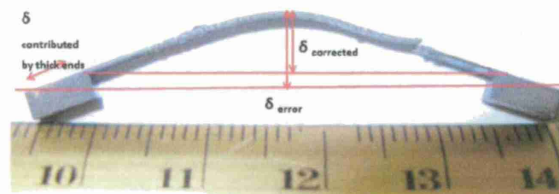


Figure 25. Image of deformed ribbon illustrating the error caused by including the contribution from thick ends to the deflection calculation.

Figure 26 plots the evolution of the corrected deformation profile of a sample undergoing creep at 1650°C under 45 MPa stress. This sample behaved as a pinned – pinned beam. The maximum deformation was plotted as a function of time. The corresponding strains were also plotted as a

function of time to derive the average creep rate. Figure 27 plots the deformation and strains in the same sample.

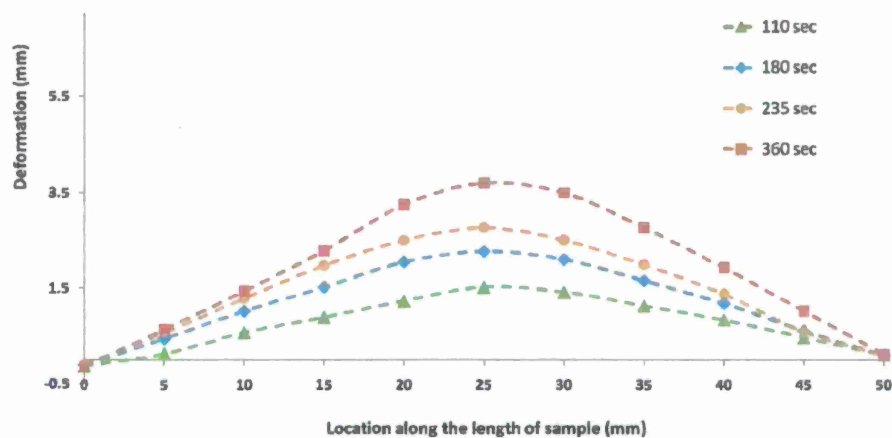


Figure 26. Deformation profile of a sample while undergoing creep at 1650 °C under 45 MPa stress. Measurements were taken using the laser micrometer.

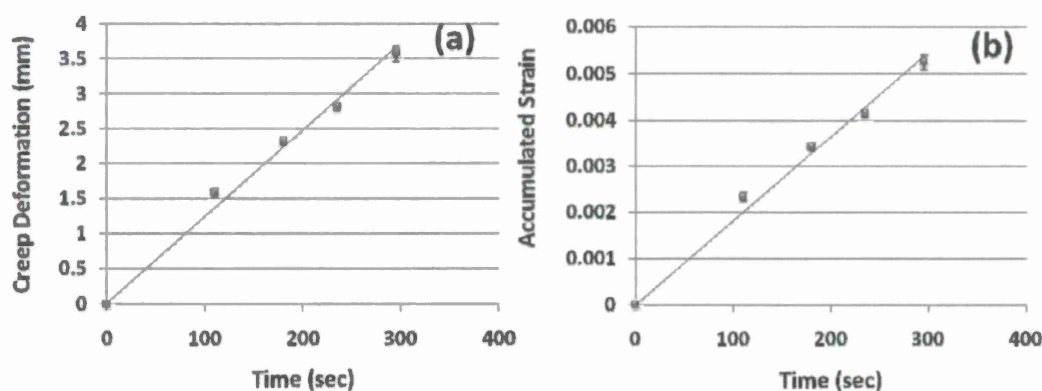


Figure 27. 1600°C under 45 MPa stress (a) center deflection δ_{max} as a function of time (b) Corresponding plastic strain. Slope of the graph was taken to be the creep strain rate of $1.7 \pm 0.1 \times 10^{-5}$ /sec.

Notice that the measured δ_{max} increases linearly with time which is taken as evidence of steady state creep. The calculated strain rate was $1.7 \pm 0.1 \times 10^{-5}$ /sec with the uncertainty based on the largest and smallest slopes consistent with this data.

4.5.4 Creep Data in Ambient and Reduced Oxygen Atmospheres

Creep data over a range of temperatures (1600-2200°C) was collected at different levels of applied stress – 20, 30 and 50 MPa. For each stress level, experiments at 5 or 6 temperatures were conducted from 1700-2200°C. For each temperature and stress condition, 2 specimens were tested. The data is in Arrhenius representation with the logarithm of strain rate plotted as a

function of inverse of temperature, to derive the activation energy from the slope. The general creep rate equation, is given by Norton-Arrhenius Equation:

Figure 28 presents the creep strain rates in air of ZrB₂-30% SiC.

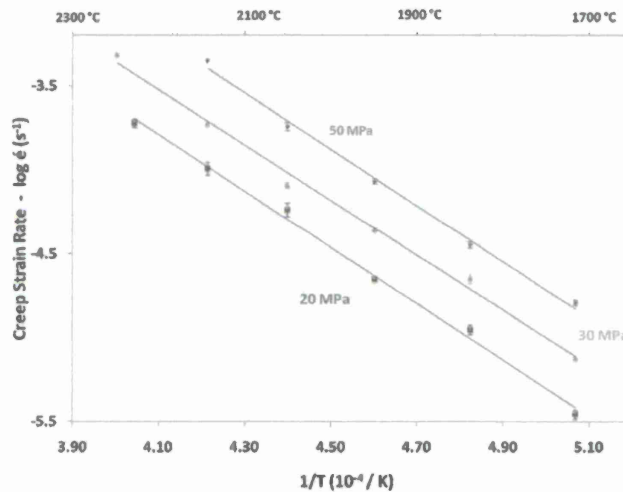


Figure 28. Creep strain rates of ZrB₂-30% SiC in air at 1700 – 2200°C under 20-50 MPa.

The data was fit with least squares regression lines and their coefficient of determination $R^2 > 0.99$. The corresponding residual sum of squares (RSS) values were used to estimate the standard deviation for the apparent activation energy derived from the slopes of these lines. The apparent activation energy was 321 ± 25 kJ/mol for 50 MPa, 313 ± 33 kJ/mol for 30 MPa and 322 ± 30 kJ/mol at 20 MPa, with the range of uncertainty calculated from the RSS. These values are statistically indistinguishable, so we can average them to estimate the apparent activation energy as 319 ± 30 kJ/mol.

The results were repeatable as observable from the small error bars which show the range of observed creep rates in the 2 independent experiments. The largest deviation (~11%) was for 2200°C/20 MPa experiment.

The stress dependence of isothermal creep is presented in Figure 29 as plot of logarithm of strain rate as a function of logarithm of stress at different temperatures.

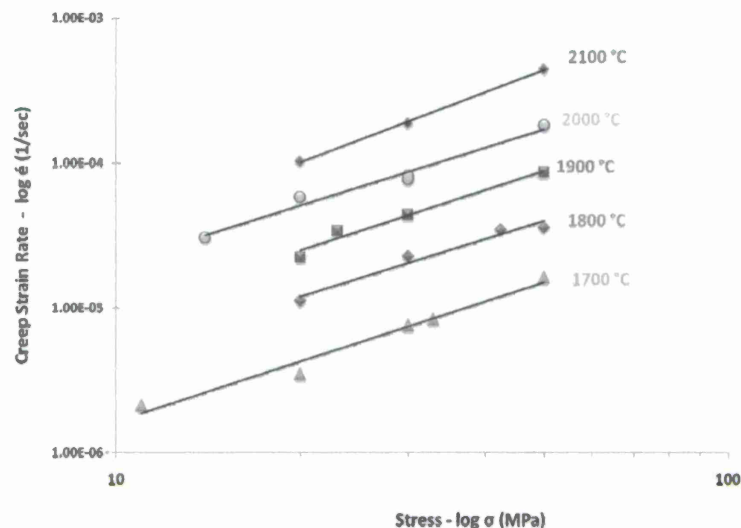


Figure 29. Logarithm of creep strain rates of ZrB_2 -30% SiC in air at 1700 – 2200°C as a function of logarithm of stress.

The slopes of these graphs correspond to the stress exponent, n . $\log \epsilon$ vs. $\log \sigma$ was rather linear at all the temperatures with the stress exponent (n) being 1.37 at 1700°C, 1.31 at 1800°C, 1.38 at 1900°C, 1.32 at 2000°C and 1.61 at 2100°C. Their average of n is 1.40 ± 0.20 . Creep experiments by previous researchers (Talmy) showed a value of $n = 1$ in ZrB_2 with 0-25% SiC. The observed stress exponent from our creep experiments 1.4 ± 0.2 is close to this literature value. This suggests that lattice creep by dislocation motion (which usually has large stress exponents) is not the dominant mechanism. It is more likely a grain-boundary or intergranular creep mechanism.

Oxidation occurs when creep testing ZrB_2 -SiC in ambient air. To understand the mechanical response of the pure ZrB_2 -SiC without the effects of oxidation, creep experiments were performed in reduced oxygen atmosphere. The oxygen content in this atmosphere was $< 0.25\%$. In this environment, the oxidation of ZrB_2 -SiC was suppressed. The creep strain rates in this oxygen starved atmosphere are presented in Figure 30 in the temperature range of 1600-2000°C at two stress levels 30 and 50 MPa.

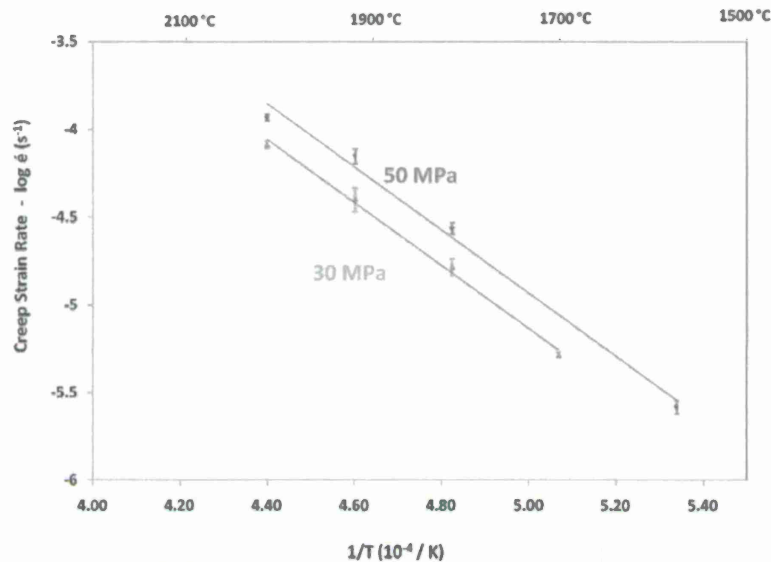


Figure 30. Creep strain rates of ZrB_2 -30% SiC in oxidation suppressed atmosphere of N_2 -0.25% O_2 at 1600-2000°C under 30-50 MPa stress.

The coefficient of determination was $R^2 > 0.99$ and the slopes of the lines corresponded to activation energies of 343 ± 24 kJ/mol at 30 MPa and 344 ± 35 kJ/mol at 50 MPa. This apparent activation energy was higher than that the value obtained for creep in air, which was 319 ± 30 kJ/mol, which corresponds slightly lower strain rates in the absence of oxidation, as can be seen from comparison of creep rates in the two atmospheres at 50 MPa stress presented in Figure 31.

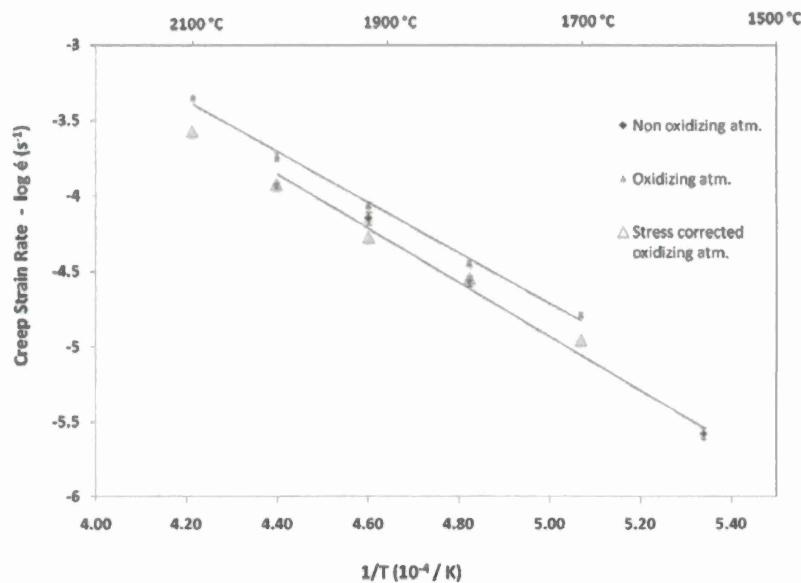


Figure 31. Comparison of creep strain rates of ZrB_2 -30% SiC in oxidizing and non oxidizing atmospheres at 50 MPa stress. The creep rates in air corrected to compensate the higher true stresses are also marked.

Since creep in air involves oxidation and oxidation reduces the thickness of the load bearing portion resulting in higher true stresses, the air creep rates need to be compensated for the

increase in stress. This is done by measuring the oxide scale thickness and correcting the nominal stress, $\sigma_{nominal}$ with this geometric factor in thickness to find the true stress, σ_{true} .

$$\sigma_{true} = \sigma_{nominal} \frac{t^2}{(t - 2t_{oxide})^2}$$

where t is the thickness of the original ribbon and t_{oxide} is the thickness of oxide scale on each surface of the ribbon. Then the stress exponent “ n ” is used to obtain the corrected creep rates, $\dot{\epsilon}_{true}$ at the nominal stress value from the measured creep rates.

$$\dot{\epsilon}_{corrected} = \dot{\epsilon} \left(\frac{\sigma_{nominal}}{\sigma_{true}} \right)^n$$

In the Figure 31, these “corrected” creep rates in air are presented along with the measured creep rates in air and $N_2 + 0.25\% O_2$. Once corrected, it was noted that these values were found to closely match the creep rates in non-oxidizing atmosphere. Since the difference between the creep rates in air vs. 0.25% oxygen can be related to geometry, it is likely that creep is not directly affected by atmosphere. A better estimate for the activation energy for creep would be the non-oxidizing value of 344 ± 35 kJ/mol.

4.5.5 Validation of Flexural Creep in ZrB₂-SiC

Weiderhorn et. al. [1999] showed that materials with glassy boundaries have much slower creep in compression, often a Norton power law, but much faster creep in tension. These are referred to as “asymmetric” materials. The tensile creep is accompanied by cavitation and does not have a power law of stress dependence. If force-fitted to a power law, it has a non-physically large stress exponent. Examples of such materials are ordinary alumina with silicate grain boundary phase and ordinary liquid phase Si_3N_4 .

During flexural bending, the outer side experiences tensile stresses and the inner side experiences compressive stresses. In asymmetric materials, since the creep laws are different on the tensile and compressive sides, the neutral axis shifts and the stress state becomes complex. Often in these cases, force-fits to Norton laws result in large apparent stress exponents.

Our creep data suggests ZrB₂-SiC has symmetric creep since the observed stress exponent was close to 1. The data points were also well fit to trend lines. This would not be possible if the material was creeping asymmetrically.

Additionally, the microstructure of the creep tested materials did not show noticeable cavitation or macroscopic amounts of grain boundary glassy phases. The UHTC research group at Imperial College London have studied the TEM of a sintered 10% SiC composite and have also observed clean grain boundaries. Therefore, the ZrB₂-SiC composites do not seem to have the viscous phases that Si_3N_4 and such materials which is the root cause for the faster tensile creep and the resultant creep asymmetry.

4.5.6 Comparison with Conventional Data

Validation of the creep data collected using the EMMA-2 and validation of the technique itself requires comparison of our data with conventionally acquired creep data of similar material with similar processing conditions. Talmy et. al. at Naval Surface Warfare Center Carderock Division (NSWCCD) had earlier studied the creep behavior of ZrB_2 -SiC composites through 4 point flexure in air as a function of temperature, stress and SiC composition. The drawback of this study was that it was limited to a rather narrow temperature range of 1300-1500°C which was also much lower than the expected application temperature. Nevertheless, our creep data was found to be highly linear with $1/T$ over a large temperature range 1600-2200°C. The small stress exponent $n=1.4$ indicates the creep mechanism might be diffusional. Talmy et al. also suggest a diffusional creep mechanism to be dominant in the temperature range they were testing. Thus, it is reasonable to extrapolate the trend lines of our data to lower temperatures for comparison purpose.

Recently, K.W. White et. al. at University of Houston also started working on creep of ZrB_2 -SiC using 4 point flexure in air as well as oxidation protected atmosphere with Ar. Their temperature range was 1400-1800°C which was certainly broader than NSWCCD. Finally, the UHTC research group at Harbin Institute of Technology in China found that their 30% SiC in 3-point flexure had a flow stress of 36 MPa at 1800°C while deforming at a constant strain rate of 4.86×10^{-5} /s. While these researchers have achieved creep data at higher temperatures than Talmy, their highest temperature is still lower than application temperatures which are expected to be >2000°C. The comparison of creep data from EMMA with the conventional data from other researchers is presented in an Arrhenius representation in Figure 32.

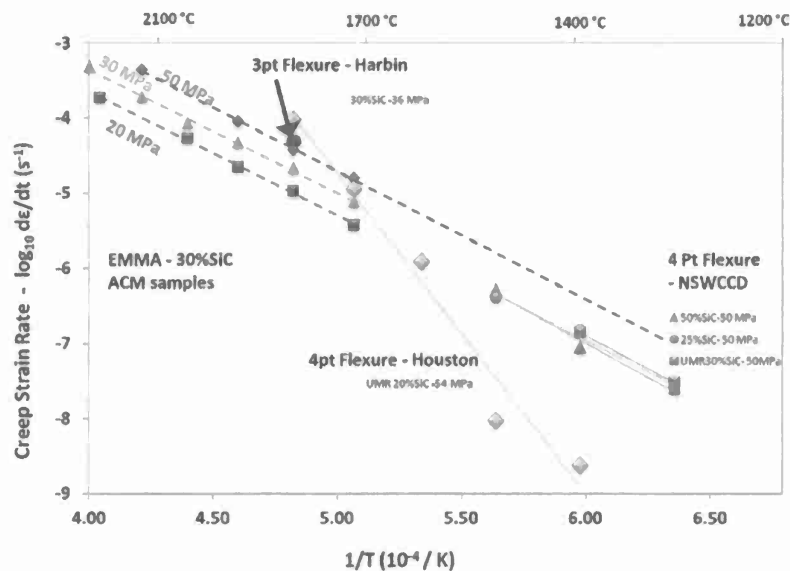


Figure 32. Comparison of EMMA creep data with conventional data acquired through 3-point and 4-point flexure.

The comparison shows that the high temperature data from Houston and the data point from Harbin group fall in the EMMA testing range. The data point from Harbin and the 1700°C and 1800°C data points from Houston almost overlap with EMMA data. The NSWCCD data by Talmy et. al. with different compositions of SiC all had similar creep rates in their temperature range of testing. The extrapolation of EMMA's 50 MPa stress line to lower temperatures shows that their data has very similar activation energy due to the similar slopes. But NSWCCD data was slower by half-an-order of magnitude.

On the other hand, the two Houston data points at lower temperatures were much slower than our predicted trend line and in fact slower even than NSWCCD data. These two data points suggest creep rates of $\sim 2 \times 10^{-9}$ /sec at 1400°C and 10^{-8} /sec at 1500°C. Their activation energy was much larger than EMMA and NSWCCD. While there are many possible reasons for why these small discrepancies, including the differences in processing of the material, SiC composition, grain boundary phases etc., altogether the creep data from EMMA is comparable to conventionally acquired data.

4.5.7 Summary

EMMA-2 now incorporates an electro-magnet, a laser deflectometer, a gauss meter, a dedicated DC power supply, basic environmental control, and each component is mounted into a rigid assembly. These system upgrades allow improved control of test variables (current, magnetic flux density, temperature, and oxidation) and improved data acquisition of sample deflections. This EMMA-2 prototype will be transitioned to ACM.

Creep will be a dominant phenomenon in UHTCs at temperatures close to 2000°C as we found through our creep experiments in this temperature range with large strain rates $\sim 10^{-5}$. Creep tests were performed both in air as well as reduced oxygen atmosphere to compare the effect of oxidation.

The directly controllable test conditions in EMMA are current and magnetic flux density. These can be maneuvered to achieve creep tests over a wide range of temperatures, 1600-2200°C under different stress conditions 20-50 MPa. This exceeds the highest temperature of testing reported in the literature. Significant deformations were observed in the long thin ribbon specimens even at relatively low strains 0.1-1%. The deformation profile of the ribbons was tracked at the maximum deformation as a function of time to derive the creep rates.

The creep from EMMA fit well with the Norton-Arrhenius law, with strain rates $\sim 10^{-6}$ at low temperatures to 10^{-4} at high temperatures. The activation energy of our 30% SiC composite was found to be 319 kJ/mol in air and 344 kJ/mol in Nitrogen. The higher activation energy in Nitrogen indicates creep rates will be faster in air. Creep testing in air caused oxidation of the UHTC and formation of oxide scales which did not support the mechanical load. This caused higher true stresses in the remaining UHTC, hence faster creep. The corrected creep rates in air (for the higher true stresses from oxidation) and the creep rates in Nitrogen were found to be very closely matching. The other kinetic creep parameter, stress exponent, was found to be 1.4.

Validation of EMMA-2 as a creep technique was done through comparison of our data with conventional data. This comparison showed that the few data points other researchers had in our testing temperature range were similar and extrapolation of EMMA trend line to lower temperatures was also similar, thereby establishing EMMA as a functional technique for high temperature creep of UHTCs.

4.6 Post Creep Microstructural Investigation

4.6.1 Motivation

There are several motives for investigating the microstructure of the material after creep experiments. The post creep specimens hold evidence of damage induced by mechanical loading during the test. The damage may be in the form of fissures or cracks in the interior of the material or grain elongation along the direction of the stress etc and can result in deterioration of the properties of the material. This is of interest for applications such as reusable thermal protection systems where the same component is expected to perform in more than one service. Even if the original material has the mechanical strength/resistance to sustain the initial use, if the material properties deteriorate during that service and the component might not be able to sustain later uses. So while the microstructure of the post creep specimens is of interest for the mechanically induced damage, there are also other motivational factors:

- a. Wiederhorn et. al. found asymmetry in tensile creep and compressive creep rates which leads to shift in the neutral axis of the specimen under flexure. Formation of cavitations at the grain boundaries (in tension) in Si_3N_4 , Siliconized SiC, and SIALON materials caused the creep rates in tension to be much faster than in compression. $\text{ZrB}_2\text{-SiC}$ flexural creep samples should verify the presence or absence of this cavitation.
- b. Creep in air at high temperatures involves oxidation of the surface of the specimens. Researchers working on the oxidation resistance of the $\text{ZrB}_2\text{-SiC}$ composite have discovered complex oxide scales including a silica liquid layer which induces a certain degree of oxidation resistance. But the oxidation resistance of the material might deteriorate during the test due to the mechanical stresses involved. The load can cause cracks/fissures in the material exposing the material underneath the oxide scales to ambient oxygen.
- c. EMMA testing exploits uniform loading in flexure, so there differential stresses exist across the thickness of the sample, with the stresses being tensile on one surface and compressive on the other surface. The effect of the nature of the stresses, tensile or compressive, and the amount of the stress on the oxidation resistance can be explored.

- d. Creep experiments performed in the environmental chamber under reduced oxygen atmosphere may result in a different kind of oxidation. The lower partial pressure of oxygen can lead to active oxidation of silicon carbide forming silicon monoxide gas. During oxidation in air, it is the passive oxidation of SiC forming silica that acts as a protective film over the surface preventing excessive oxidation. In the absence of the silica oxide scale, the oxidation resistance will be lower. On the other hand, the partial pressure of the oxygen could be too low for the oxidation of ZrB_2 . So the result of these two countering effects of lower oxygen partial pressure can be studied.

The surfaces of post creep specimens are covered in oxide scales which form during testing. To access the internal microstructure, samples were sectioned to obtain two types of cross sections – one across the length (axial) and one cut along the length (transverse). Both sections were made near the middle of the ribbon where the stresses are highest. Both cross sections can be used to compare the compressive and tensile side of the sample and to seek evidence of damage from mechanical loading in the interior sample beneath the oxide scales.

The axial cross section shows microstructure along the two dimensions, thickness (t) and width (W), both of which experience no stresses in ideal flexure. The transverse cross section on the other hand shows microstructure along the length direction (L) which experiences maximum stress at the middle of the ribbon. Therefore, this cross section can be utilized to explore the damage induced by the stresses in the form of grain elongation. If the mechanical loading during the testing at high temperature caused grain softening and eventual grain elongation, it can be quantified using the ratio of the length of the grains along the length dimension and the grain length along thickness dimension near the tensile surface.

4.6.2 Post Creep Specimens' Microstructure: Air

The specimens tested in air had the typical oxide scales such as shown in Figure 33. This is a post creep specimen exposed 300 seconds in air at 1800°C under 38 MPa stress. There is an outer silica glass layer 10 μm thick, a primary ZrO_2 layer 27 μm thick, and a porous ZrB_2 layer 33 μm thick which is SiC depleted. The ZrO_2 and ZrB_2 have similar contrast and appear in brighter shade in the secondary electron image. The SiC and SiO_2 with lower atomic weight appears in darker contrast. The void spaces in the porous ZrB_2 appear in a much darker contrast.

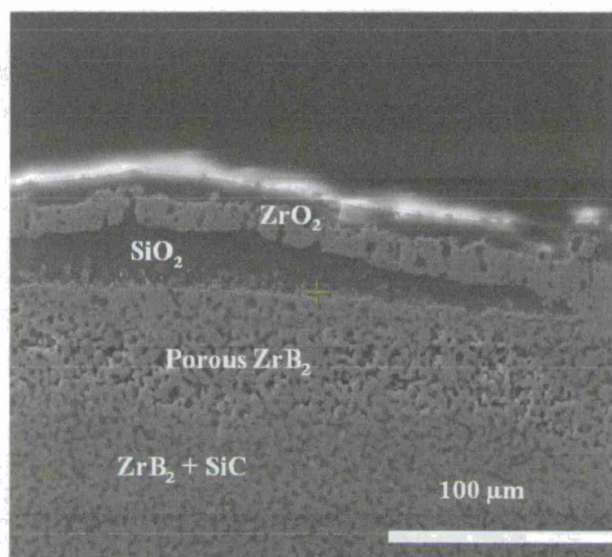


Figure 33. Secondary electron image of the oxide scale in a specimen creep tested at 1800°C under 38 MPa stress in Air for 300 seconds to a creep strain of 0.37%.

In these post creep specimens tested in air, cracks were observed in the oxide scales between the ZrO_2 -Silica glass scale and porous ZrB_2 in the SiC-depleted layer, as shown in Figure 34. The cracks are not associated with the mechanical loading in creep, since they are present even in the specimens simply resistively heated with no magnetic field. In the latter samples, only oxidation occurred without any mechanical load. Figure 35 shows the cross section of the sample with similar crack located precisely between ZrO_2 -Silica glass scale and porous ZrB_2 in the SiC-depleted layer.

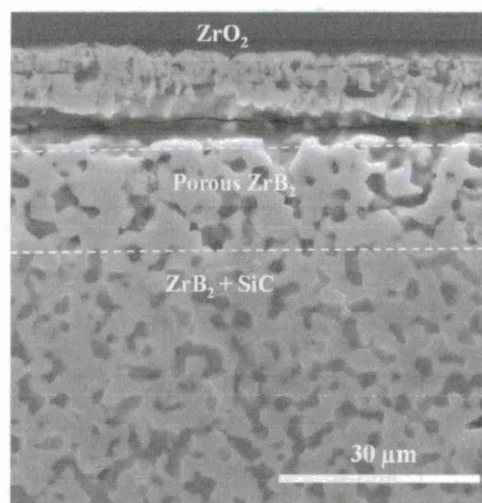


Figure 34. Cracks between ZrO_2 and porous ZrB_2 oxide scales of sample creep tested in air at 1700°C under 30 MPa stress to a final strain of 0.445%.

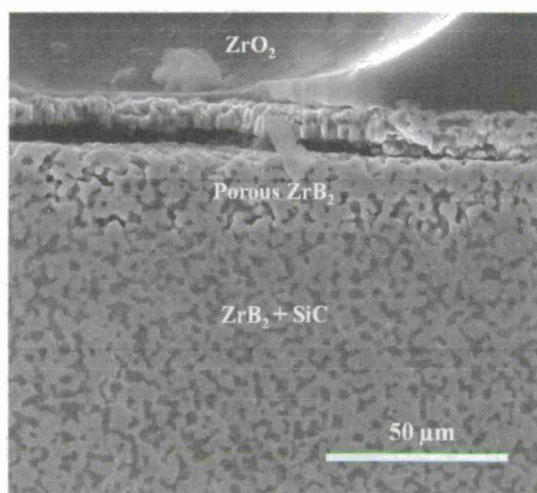


Figure 35. Cracks developing into delamination in the sample resistively heated in air to 2000°C.

The cracks are not associated with thermal shocks from the exceeding fast heating and cooling rates from the ribbon method, since they also are seen resistively heated with slow ramp rates (30°C/s). A plausible explanation for occurrence of cracks between the zirconia oxide scale and the ZrB_2 substrate is the phase transformation of Zirconia from tetragonal, the stable phase at the temperatures of creep test, to monoclinic crystal structure during cool down. Evidence in Figure 35 supports this possibility since the cracks developed into a delamination where the delaminated portion is longer than the substrate, indicating expansion in the oxide scale.

The crystalline phase of ZrO_2 in the oxide layer was confirmed to be monoclinic Zirconia through X-ray diffraction (Rigaku Rotating Anode X-Ray Diffractometer). X-ray diffraction analysis of the surface of the ribbon specimens tested at lower temperatures in air had diffraction peaks corresponding to Monoclinic ZrO_2 (Figure 36). The large volume expansion associated with the tetragonal-monoclinic transformation during cooling is therefore concluded to be the cause for the cracks between the oxide scale and for the Zirconia oxide layer to detach/delaminate from the rest of the substrate.

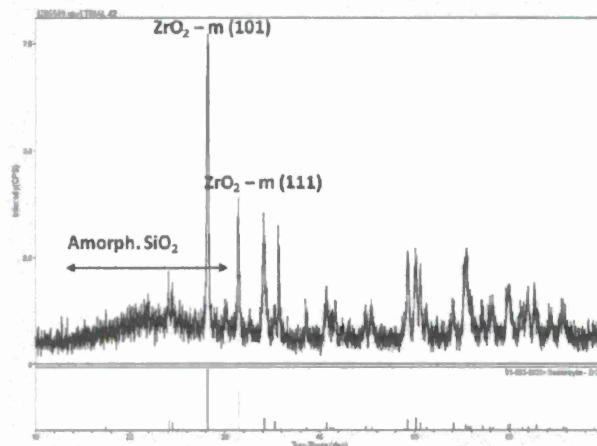


Figure 36. X-Ray Diffraction pattern of the surface of the oxide scale of a sample creep tested in air.

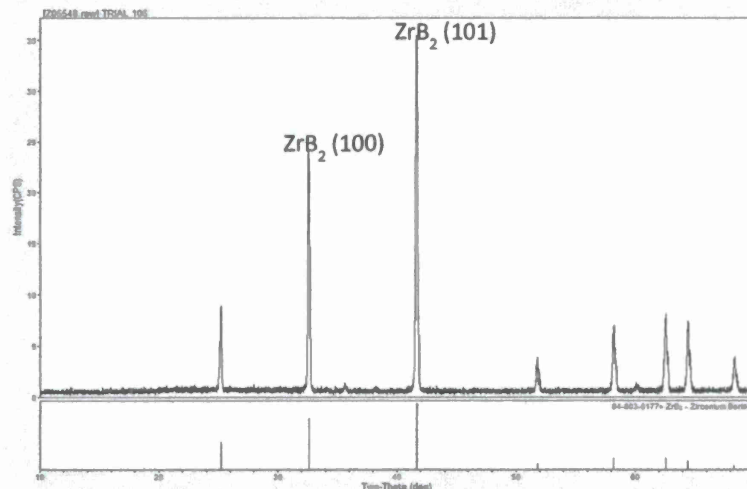


Figure 37. X-Ray Diffraction pattern of the surface of the sample creep tested in reduced oxygen atmosphere.

4.6.3 Post Creep Microstructure – Reduced Oxygen Atmospheres

The samples tested in reduced oxygen atmosphere in the environmental chamber showed a surface layer very unlike the traditional oxide scales seen in the samples tested in air. It did not have any silica or the porous ZrB_2 layer. It showed a uniform dense microstructure of similar contrast as the ZrB_2 in the UHTC. It had a thickness of $<5 \mu\text{m}$ much smaller than the $50\text{-}100 \mu\text{m}$ thick oxide scales seen in air. This crystalline phase had a grain size comparable to the original material and was identified using X-Ray Diffraction analysis (Figure 37) of the surface of the ribbon specimen as ZrB_2 . The pattern had diffraction peaks corresponding to ZrB_2 such as (101) at $2\theta = 41.6^\circ$, (100) at $2\theta = 32.6^\circ$ etc. But compared to the specimen thickness this is only about 1.5% and would not affect creep behavior. Figure 38 shows a specimen tested in the 0.25%

oxygen atmosphere at 2000°C under 50 MPa for 75 seconds, which had only a 5 μm thin scale of ZrB_2 on its surface. This zirconium diboride surface scale could be a result of depletion of SiC from active oxidation of SiC on the surface.

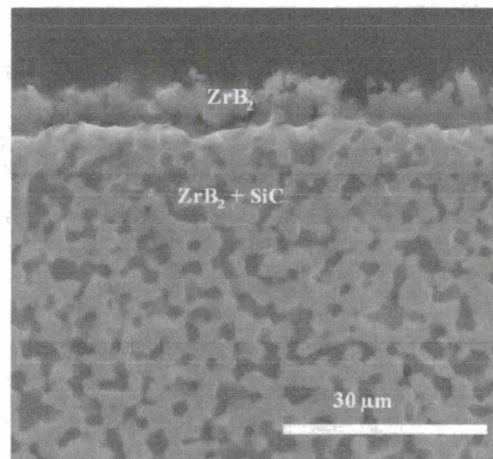


Figure 38. Specimen tested at 2000°C under 50 MPa stress for 75 seconds to a final strain of 0.86% in air with 0.25% O_2 .

4.6.4 Post Creep Microstructure – Damage Evidence

In both the creep tests in air as well as in reduced oxygen atmosphere, the microstructure of the unreacted ZrB_2 -SiC seemed unaffected. No evidence of internal damage such as cracks or fissures were observed which indicates the material is resilient to creep strains up to 1%. Figure 39 is a secondary electron image of a region close to the tensile surface of the ribbon in the cross section cut along length. The specimen was creep tested at 2000°C under 50 MPa stress in non-oxidizing atmosphere with a final strain of 0.86%, which is one of the largest total strains for our specimens.

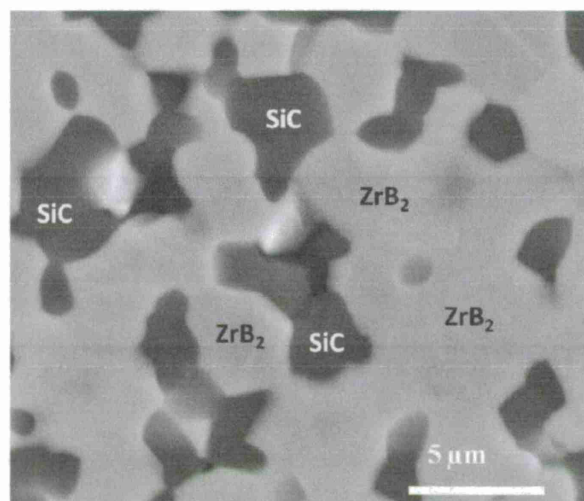


Figure 39. Secondary electron image of the cross section of sample creep tested at 2000°C under 50 MPa stress in 0.25% O₂ to a final strain of 0.86% near tensile surface shows no damage in ZrB₂ or SiC grains.

In pure flexure where there is no strain in width/thickness, differential strains in the length direction are at maximum at the surface. Therefore, the effect of flexural strain on the microstructure would be most noticeable at the tensile surface. However, there was no damage observed such as cracks or fissures or obvious grain elongation.

The absence of noticeable cavitation or macroscopic amounts of glassy phases at the grain boundaries indicates that the hot pressed ZrB₂-SiC behaves differently than the cavitation-prone Si₃N₄, siliconized SiC and SIALONs studied by Wiederhorn et. al. The ZrB₂-SiC will therefore be free from the issues of creep asymmetry that arises from cavitation and glassy phases. In fact, the same researchers (Wiederhorn et. al.) have observed that non-cavitation tensile creep in Lu-doped Silicon Nitride showed similar creep rates on both sides of flexure.

Although there was no change in the grain shape perceptible to the naked eye, creep could have elongated the grains in the tensile direction. Linear intercept measurements of ZrB₂ and SiC grain lengths were performed. There was no verified directional elongation along length, as shown in Figure 40. ZrB₂ grains were about $2 \pm 0.5 \mu\text{m}$ and the SiC grains were about $1.5 \pm 0.5 \mu\text{m}$ in size.

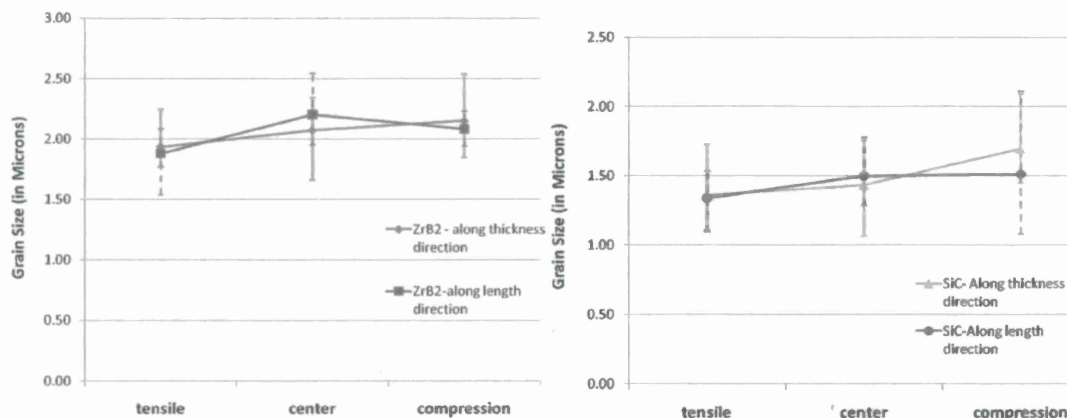


Figure 40. Grain lengths of ZrB₂ (Left) and SiC (Right) grains along thickness and length directions in tensile, center and compressive regions of the flexure.

The absence of grain elongation along the stress direction indicates the creep mechanism is not associated with intragranular flow or diffusion. While the small stress exponent indicates Newtonian flow, the secondary electron microscope images did not show observable cavitation or macroscopic amounts of glassy phase. Therefore, it is not clear at this point as to what the main deformation mechanism is. Transmission Electron Microscopy (TEM) studies would be needed to investigate the grain boundaries for evidence of deformation.

4.6.5 Eutectic Melting in ZrB₂-SiC

Creep tests were not successful above a surface temperature of 2210°C due to eutectic melting of the ZrB₂-SiC. Despite the high melting temperatures of the UHTC ZrB₂ (3246°C), addition of SiC lowers the melting point of the composite by almost 1000°C to 2270°C. A phase diagram calculated by Kauffman shows a eutectic in the ZrB₂-SiC system at 2270°C around 54 wt% ZrB₂. (Figure 41)

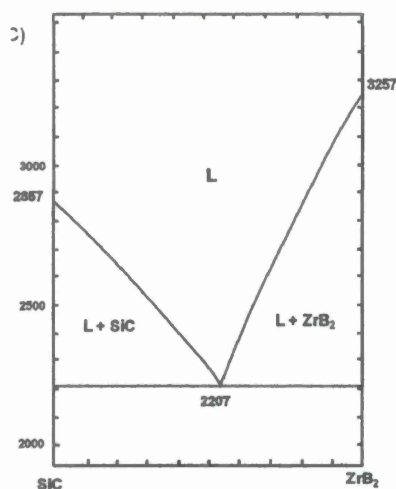


Figure 41. Eutectic in the ZrB₂-SiC Phase Diagram at 2207°C.

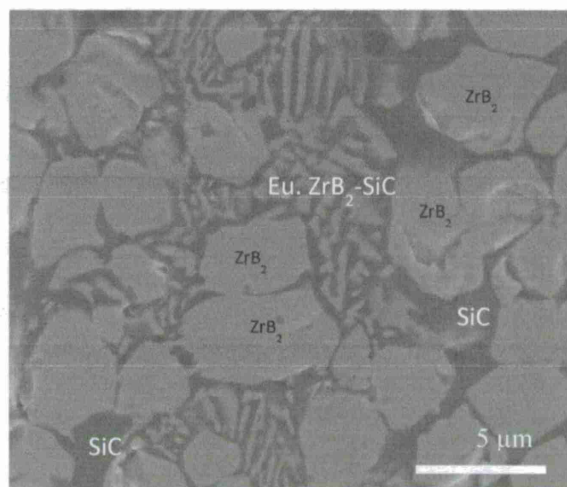


Figure 42. Secondary electron image of the lamellar microstructure from eutectic melting at 2210°C.

Above this eutectic temperature, these ZrB_2 -30 V% SiC composites should consist of proeutectic ZrB_2 solid with about 40% eutectic liquid. Figure 42 shows the microstructure in the sample heated to a surface temperature of 2210°C and cooled down to room temperature. It displays a classic eutectic microstructure with lamellar eutectic zirconium diboride grains about 1 μm in thickness in a SiC matrix. Some of the ZrB_2 grains were still intact while many of them seem to have been partially reacted with the eutectic. All the SiC grains have lost their shape definition, suggesting that they were melted in the eutectic liquid. The melting caused the ribbon to rupture, ceasing current flow for the resistive heating. So while EMMA is capable of creep testing UHTCs at higher temperatures, it is the specimen melting (in this case) which prevents creep testing at temperatures near the eutectic point.

4.6.6 Summary

The microstructure of post creep ZrB_2 -30% SiC specimens tested using EMMA at ultra high temperatures was studied for understanding the effect of oxidation as well as evidence of damage from mechanical loads.

Specimens tested in oxidative environment (ambient air) showed extensive oxidation resulting in complex oxide scales composed of an outer layer of Silica and Zirconia underneath which is a porous ZrB_2 layer formed from selective oxidation of SiC. The microstructure of the oxide layers was comparable to conventionally furnace tested specimens studied by other researchers. Cracking and delamination were observed in these oxide scales between the outer Zirconia layer and the inner porous ZrB_2 layer. They were discovered to originate from the phase transformation of Zirconia formed in tetragonal during high temperature of testing to monoclinic crystal structure during the cool down. Specimens tested in the environmental chamber in non-oxidative environment (Nitrogen and 0.25% O_2) confirmed oxidation suppression. No oxide scales were observed. Only a 5 μm thin outer layer of ZrB_2 was observed resulting from a small amount of active oxidation of SiC from surface.

Investigation of inner microstructure of unreacted material was done through axial and transverse cross sections. No evidence of damage such as cracks or fissures was discovered. Grain size measurements comparing the grain length along the loading direction (length) with grain length along non-strain direction (thickness) were done. The material showed no elongation of ZrB_2 or SiC grains in these specimens deformed to 1% strain and at very high temperatures 2100°C. But the specimens tested above 2200°C showed excessive damage from melting. The microstructure showed lamellae structures and pro-eutectic ZrB_2 grains indicating eutectic melting which was corroborated through the phase diagram of the ZrB_2 -SiC composite. EMMA is capable of creep testing UHTCs at temperatures >2200°C but the test specimen composed of ZrB_2 -SiC melted at these extreme temperatures.

5.0 CONCLUSIONS

EMMA-2 was successfully designed and realized. The second generation creep characterization system now integrates an electro-magnet, a laser deflectometer, a gauss meter, a dedicated DC power supply, basic environmental control, and each component is mounted into a rigid assembly. These system upgrades allow improved control of test variables (current, magnetic flux density, temperature, and oxidation) and improved data acquisition of sample deflections. This EMMA-2 prototype will be transitioned to ACM.

The directly controllable test conditions in EMMA are current and magnetic flux density. These can be maneuvered to achieve creep tests over a wide range of temperatures, 1600-2200°C under different stress conditions 20-50 MPa. This exceeds the highest temperature of testing reported in the literature. Significant deformations were observed in the long thin ribbon specimens even at relatively low strains 0.1-1%.

The creep from EMMA fit well with the Norton-Arrhenius law, with strain rates $\sim 10^{-6}$ at low temperatures to 10^{-4} at high temperatures. The activation energy of our 30% SiC composite was found to be 319 kJ/mol in air and 344 kJ/mol in Nitrogen. The higher activation energy in Nitrogen indicates creep rates will be faster in air. Creep testing in air caused oxidation of the UHTC and formation of oxide scales which did not support the mechanical load. This caused higher true stresses in the remaining UHTC, hence faster creep. The corrected creep rates in air (for the higher true stresses from oxidation) and the creep rates in Nitrogen were found to be very closely matching. The other kinetic creep parameter, stress exponent, was found to be 1.4.

Specimens tested in the environmental chamber in non-oxidative environment (Nitrogen and 0.25% O_2) confirmed oxidation suppression. No oxide scales were observed. Only a 5 μm thin outer layer of ZrB_2 was observed resulting from a small amount of active oxidation of SiC from surface.

Investigation of inner microstructure of unreacted material was done through axial and transverse cross sections. No evidence of damage such as cracks or fissures was discovered. Measurements of post creep samples showed no elongation of ZrB_2 or SiC grains in specimens deformed to 1% strain and at very high temperatures 2100°C. But the specimens tested above 2200°C showed excessive damage from melting. The microstructure showed lamellae structures and pro-eutectic

ZrB₂ grains indicating eutectic melting which was corroborated through the phase diagram of the ZrB₂-SiC composite.

EMMA is capable of creep testing UHTCs at temperatures >2200°C but the test specimen composed of ZrB₂-SiC melted at these extreme temperatures.

Validation of EMMA-2 as a creep technique was done through comparison of our data with conventional data. This comparison showed that the few data points other researchers had in our testing temperature range were similar and extrapolation of EMMA trend line to lower temperatures was also similar, thereby establishing EMMA as a functional technique for high temperature creep of UHTCs.

Creep will be a dominant phenomenon in UHTCs at temperatures close to 2000°C. The progress in system development and early test results are significant to the high temperature materials community because it offers a rapid low cost test system to perform creep measurements at 2400°C+. EMMA based testing would be relevant for hypersonic vehicles in the DOD arsenal as well as commercial space launch vehicle. We believe an EMMA can be readily modified to conduct additional (non-creep) mechanical testing of UHTMs of interest to the high temperature materials community.

6.0 REFERENCES

N/A

LIST OF ACRONYMS, ABBREVIATIONS, AND SYMBOLS

ACM	Advanced Ceramics Manufacturing
EMMA-1	Electro-Magnetic Mechanical Apparatus (Phase I Prototype)
EMMA-2	Electro-Magnetic Mechanical Apparatus (Phase II Prototype)
ONR	Office of Naval Research
UHTC	Ultra High Temperature Ceramic
UHTM	Ultra High Temperature Material